Hindawi
Adsorption Science & Technology
Volume 2022, Article ID 4421932, 28 pages
https://doi.org/10.1155/2022/4421932

Research Article

Structural Alteration, Hydration Stability, Heavy Metal Removal Efficiency, and Montmorillonite Porosity Fate by Coupling the Soil Solution pH and a Thermal Gradient

Chadha Mejri, Walid Oueslati, and Abdesslem Ben Haj Amara

Université de Carthage, Faculté des Sciences de Bizerte, LR19ES20: Ressources, Matériaux, Et Ecosystèmes (RME), 7021 Bizerte, Tunisia

Correspondence should be addressed to Walid Oueslati; walidoueslati@ymail.com

Received 9 June 2022; Revised 28 July 2022; Accepted 4 August 2022; Published 27 August 2022

Academic Editor: Linchuan Fang and Huihui Du

Clay minerals are considered as a promising material in the context of geological barrier for the confinement of radioactive and industrial waste. Understanding the usefulness of the smectite mineral, in this approach, remains insufficient. The deep investigation about structural response/changes, hydrate stability, cation exchange process, permeability, and heavy metal/radionuclide adsorption/removal efficiency under external constraints is needed. To explore the structural alteration, the hydration stability, and the evolution of montmorillonite porosity under a first order of external applied constraints coupling, a reference Na-rich montmorillonite specimen is used as a starting material, and three exchangeable heavy metal cations (Ba^{2+}, Cu^{2+}, and Co^{2+}) have been selected. The applied constraint coupling is realized at laboratory scale and assured by simultaneously varying of the soil solution pH and the thermal gradient. The evaluation of the mineral fraction response is established by correlation of quantitative XRD analysis results, thermal analysis, and porosity measurements. The quantitative XRD analysis allows rebuilding of the theoretical model describing the interlamellar space (IS) configurations/damages, structural heterogeneity degrees, and hydrous stability. Obtained results show a dominant interstratified hydration character, for all studied complexes, attributed to a new IS organization versus the applied constraint strength. Furthermore, all samples exhibit a heterogeneous hydration behavior traduced by the coexistence of different layers of type population within the crystallite. Additionally, the theoretical XRD profile decomposition allowed us to prove link between the domination of the segregated stacking layers mode against the constraint strength. Thermal analysis allowed us to develop theoretical models describing the decrease of the water molecule amounts as a function of the increase in temperature and soil solution pH. Moreover, a specific hydration footprint response and an interstratification mapping are assigned for each corresponding stress degrees. The evolution of montmorillonite porosity is determined by adsorption measurement, based on Brunauer, Emmett, and Teller (BET) and Barrett-Joyner-Halenda (BJH) pore size distribution analyses which confirms for all samples, the exfoliation process, and the mesopore diameter rise by increasing the constraint intensity.

1. Introduction

Montmorillonite is a 2 : 1 phyllosilicate type belonging to the smectite family. The montmorillonite structure consists of a stack of an octahedral (O) sheet (MO_4 $(OH)_2$) where (M) can be (Al) or (Mg) ions sandwiched between two tetrahedral (T) sheets (SiO_4). This structure is labeled by T-O-T, and the associated layer thickness along the c^* axis is about 10 Å [1–4]. The montmorillonite differs from the other dioctahedral smectites (beidellite and nontronite) by the existing isomorphous substitutions which occurs in the tetrahedral sheet (i.e., Al^{3+} substitutes for Si^{4+}) rather than in the octahedral sheet [5]. Indeed, the isomorphic substitutions appearing in the (T) or/and (O) sheets are defined by the localization of different type of cations in the various cavities. These substitutions result in a load deficit that is compensated on the outside of the layer, by compensating cations (CC) [5–7]. The intrinsic montmorillonite properties find a large environmental application domain as depolluant [8–11], ion exchanger [12–16], natural geological barrier for

industrial and radioactive waste confinement [17], clay-based nanocomposite for drug delivery [18–27], cosmetic compounds [28–31], medicinal application [32–35], antibacterial properties, and as a topical treatment for skin problems [36–39]. The structural and morphological properties are at the origin of this efficiency and the great exploitability in several fields of application. Indeed, the layer type with its infinite lateral extension (2D), the interlamellar space (IS) allowing the individual layer swelling (then the swelling of the crystallites) with the possibility of solvent insertion (due to the capacity of cation exchange CEC), and the macroporosity associated with the high specific surface (SA) (external and internal) are essential assets favoring the exploitation of such minerals [40, 41]. The montmorillonite layer expansion amount is affected, respectively, by the intrinsic layer charge location, the type/size/charge of exchangeable cation, the abundance/organization of water molecule in the IS, the type/size of organic/inorganic fraction present in the contact solution, the material history (fatigue/stress/strain), and the surrounding environmental/geochemical/mechanical conditions [42–46]. The CC and water molecules are positioned inside the IS, during cation exchange process, following a discreet arrangement allowing a progressive swelling process (hydration process) confirmed by the discretization of the basal spacing distance (d_{001}) fluctuations. The literature proposed basal spacing level defined by [5, 6, 47–49] is as follows: dehydrated 0 W (d_{001}~10 Å), one water layer 1 W (d_{001}~12.4 Å), two water layers 2 W (d_{001}~15.4 Å), three water layers 3 W (d_{001}~18.2 Å), and finally, four water layers 4 W (d_{001}~21 Å).

Montmorillonite is widely exploited (in adsorption science) for neutralizing the soil heavy metal dispersion/diffusion [50–52]. The adsorption factor usually depends on the solid/liquid ratio parameters in such kind of application. Usman et al. (2004) [53] demonstrate that low doses of clay (about 4% to 8%) eliminate up to 70% of heavy metals. In addition, the increase in the dose of the clay fraction is accompanied by the increase in the rate of adsorption [54, 55]. Also, the required dose and the remediation force may be affected by the variation in the mineral structural composition [56]. In the other hand, clay plays an essential role in the basic design of deep storage sites for radioactive and industrial waste confinement process [57–60]. The architecture of the sites is achieved by the association of several types of barriers (multibarrier concept). It consists of filler which is the waste in metal packages, incubated by a thick of concrete layer, covered by a clay films buried in well-determined host rock, at a depth of about 500 m below sea level. Several reasons, like the high radioactive element's adsorption capacity and the low permeability which slows down the radionuclides migration in the host rock, detailed in the work of [61–66] are in favor of the use of clay as a geological coating.

The clay adsorption capacity and the clay permeability properties are very sensitive to the variation of the soil solution pH [67–72], the surrounding temperature gradient [56, 67, 68, 72, 73], the kinetic effect during the cation exchange process [74], the surrounding atmospheric pressure variation [75, 76], the surrounding relative humidity (RH) constraint [77–81], the solid-liquid ratio effect during heavy metal removal [41], and the type and nature of the compensating cations [82–85]. Several works [67–72] show that there is a linearly proportional relationship between the pH level fluctuation and the performance of the heavy metal absorber (clay fraction). Es-Sahbany et al. (2019) [72] show that at room temperature, an optimal value of heavy metal adsorption rate was obtained; although at slightly lower or higher temperatures, this result may still be more ideal. Chantawon et al. (2003) [86] and Usman et al. (2004) [53] demonstrate good adsorption results at relatively high temperatures of around 36°C unlike some researchers [87] that observed a decrease in the adsorption rate at temperatures above 30°C. Other authors [88, 89] have proven that chemical adsorption reactions are essentially faster for temperatures that gradually increase with continuous increases in temperature.

On the other hand, the experimental approach in the study of the interaction (adsorption, cationic exchange and intercalation) of montmorillonite with heavy metals (and even organic molecules) by XRD analysis has been confirmed by theoretical calculations. Zhang et al. (2018) [90] studied the uranyl ion complexation on montmorillonite edges using a combined first-principle molecular dynamics and surface complexation modeling approach. Obtained results in the case of four selected representative complexing sites show that uranyl ions form hydrolyzed bidentate complexes on these sites. Liu et al. (2021) [91] used the molecular dynamic simulations to explain the sorption behaviors of heavy metal ions (zinc, cadmium, and lead) in the interlayer and nanopore of Wyoming montmorillonite. The calculated diffusion coefficients of the selected three cations in interlayer and nanopore indicated that their diffusion abilities were significantly impaired, implying that montmorillonite adsorbents have a strong ability to fix and retard heavy metal ions. Zhang et al. (2022) [92] investigates by the molecular dynamic simulations of the exchange behavior of radionuclides into montmorillonite. Authors demonstrate that multivalent cations prefer to stay in the mid-plane of interlayer region, and Cs+ and Rb+ cations are located closer to the basal plane via inner-sphere complexation. Furthermore, the orientations of interlayer uranyl ions are nearly perpendicular to basal surface. Density functional theory (DFT) is used to validate XRD data in the case of hydrated Na-hectorite exchanged with Cs-, Ca-, and Sr-cations [93]. Also, the first-principle DFT provides a prediction of the structure, stability, and dynamic properties of organoclays based on montmorillonite (Mt) intercalated with two types of organic cations—tetrabutylammonium (TBA) and tetrabutylphosphonium (TBP) [94]. The Cs adsorption on montmorillonite clay is investigated by ^{133}Cs chemical shift calculations, ^{133}Cs magic-angle-spinning nuclear magnetic resonance (MAS NMR) spectroscopy, X-ray diffraction under controlled relative humidity, and DFT calculations [95]. Obtained results shows that all Cs atoms were positioned around the center of hexagonal cavities in the upper or lower tetrahedral sheets. The calculated ^{133}Cs chemical shifts were highly sensitive to the tetrahedral Al (Al^{T})-Cs distance and d-spacing, rather than to the Cs coordination number.

Work on the linkage of constraints has not been adequately addressed in the literature. Indeed, Meftah et al. (2010) [84] showed that for a well-determined pH value and at a precise temperature clay can permanently change its structure. Thus, Marty et al. (2020) [85] explained that the coupling between the chemistry and hydration of clays shows a specific behavior for most water molecules considering RH and interlamellar space composition. The constraint coupling affecting, respectively, the clay hydration behavior, the absorber performance, and the ion exchanger efficiency is timidly approached during the main works carried out in the last decade focusing the use of clay in the context of multibarrier [41, 79, 96]. Several works [41, 79, 96] have concentrated on the effect of individual parameter and neglecting the coupling and the interaction between existing/surrounding parameters which generally affect the functionality of the material. Very few works are based on this very realist approach [12, 71]. To take full advantage of the huge possibilities of use of these minerals, it is necessary to simulate, at the laboratory scale, what happens during the real use. This approach is realized by respecting a scientific methodology based on five steps. The first is to decipher the nature and intensity of the constraints affecting the mineral (in question), and secondly, to determine the order of the possible couplings constraints and their nature (e.g., first coupling order: coupling of two constraints (e.g., T-%RH, T-pH, T-CEC, S/L ratio-T, …) and second coupling order: coupling of three constraints T-pH-S/L ratio and mechanical stress-T-%RH, …). The third step is to create and implement these constraint coupling types on a laboratory scale. The fourth step is to characterize the material's response. The last step is the evaluation/optimization based on the eventual results. The tremendous combination of constraints increases the challenges. For this purpose, we will focus on this work only at the first-order coupling between soil solution pH and thermal gradient designated by (T-pH).

Essentially, this work focuses the structural alteration, hydration stability, and evolution of montmorillonite porosity by (T-pH) in the case of Na-rich montmorillonite exchanged with heavy metals M^{2+}. This necessarily requires the realization/validation at the laboratory scale of an experimental first-order coupling which consists of the variations of geochemical and thermal stresses strength simultaneously. The structural evaluation is realized by a specific quantitative XRD analysis based on the modeling of the 001 reflections. Thermal analysis is used to develop the model describing interlamellar water molecule amount evolution versus constraint strength. The adsorption specificities and the porosity growth are investigated by BET and BJH pore size distribution analyses.

2. Materials and Methods

2.1. Baseline Material. A standard dioctahedral smectite SWy-2 extracted from the cretaceous formations of Wyoming (USA) and provided by the clay mineral repository is selected for the present study [1]. The structural formula per half-cell is given by [43]:

$$\left(Si^{4+}_{3.96}, Al^{3+}_{0.04}\right)\left(Al^{3+}_{1.53}, Fe^{3+}_{0.18}, Fe^{2+}_{0.045}, Mg^{2+}_{0.26}, Ti^{4+}_{0.01}\right) \cdot O_{10}(OH)_2\left(Ca^{2+}_{0.07}, K^{+}_{0.01}Na^{+}_{0.2}\right) \quad (1)$$

This bentonite exhibits a low octahedral charge and extremely limited tetrahedral Substitutions. The clay cation exchange capacity (CEC) is 101 meq/100 g [43].

2.2. Pretreatment. A pretreatment of the starting material consists of preparing Na-rich montmorillonite suspension (SWy-Na) is realized following a classic protocol detailed by [41] as shown in Figure 1.

2.3. Exchangeable Cations. Three heavy metal cations (Ba^{2+}, Cu^{2+}, and Co^{2+}) were the subject of the cation exchange process. The cation preference is explained by the wonderful abundance of the latter in industrial and radioactive waste and the specific characteristics of each one [97].

2.4. First-Order Coupling Constraints. First-order stress coupling is based on the association of geochemical (soil solution pH) and the thermal gradients (obtained by varying T °C) at the laboratory scale. To achieve this goal, an MCl_2 solution (where M is the metal cation Ba^{2+}, Cu^{2+} and Co^{2+}) at a well-determined pH is prepared at a low concentration (0.1 M), followed by the addition of Na-rich montmorillonite powder (SWy-Na). For each constraint pair created (fixed pH and fixed T), an adjustment of the overall volume (200 mL) is made by adding the metal chloride solution and the acid or base additive. Subsequently, and after several mechanical shaking cycle, a cation exchange process will take place at a well-determined temperature for a fixed specified period (24 h) (Figure 2). The soil solution pH variation and temperature values (T°C) are carried out on the same sample. All experimental parameters are summarized in Table 1.

2.5. Cation Exchange Process. A cation exchange process is carried out for each bivalent metal cations Ba^{2+}, Cu^{2+}, and Co^{2+} brought into contact with the starting sample. The experimental protocol established for each sample consists of applying a mechanical shake throughout 48 h, followed by centrifugation at 4000 rpm. This step is repeated five times to ensure process achievement. After recovery of the solid fraction, a series of washes with distilled water will take place to remove excess of salt from chloride ions. The obtained sample is labeled SWy-M with M that is the metal cation type (e.g., SWy-Ba, SWy-Cu, and SWy-Co). The experimental protocol is summarized in Figure 3.

To be able to analyze the complexes obtained using XRD, oriented sample was prepared by placing the obtained suspensions on a glass slide at air dry for 24 h.

2.6. X-Ray Diffraction (XRD). Structural characterization is carried out using XRD analysis by a Bruker D8 ADVANCE (Bruker AXS GmbH, Karlsruhe, Germany) with CuKα monochromatic radiation ($\lambda = 0.15406$ nm) at 40 kV and 20 mA. The usual scanning parameters were 0.01 ($2\theta^{\circ}$) as the step size and 6 s as the counting time per step over the

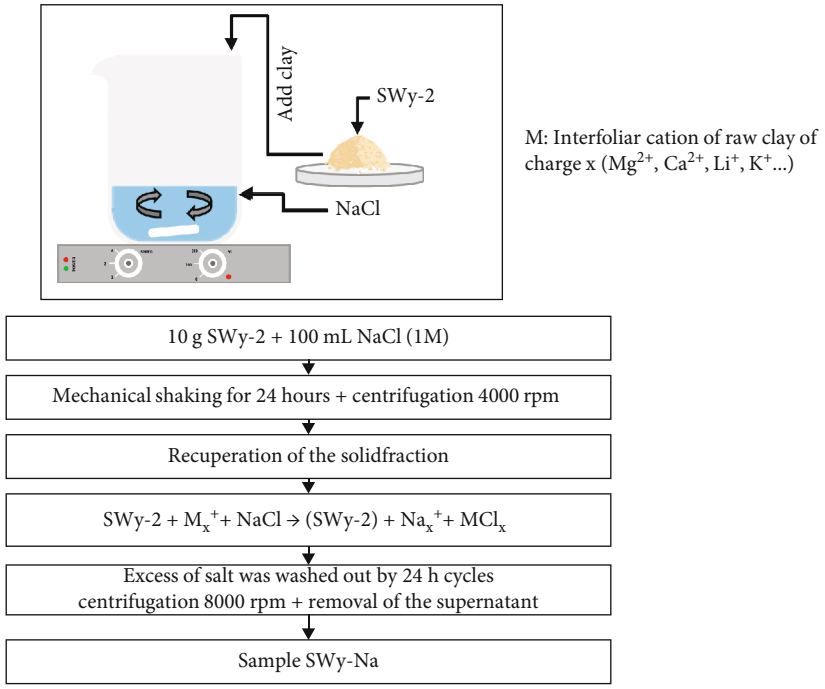

Figure 1: Experimental protocol for the purification of the starting material. Excess of salt was washed out by 24 h cycles: centrifugation 8000 rpm + removal of the supernatant.

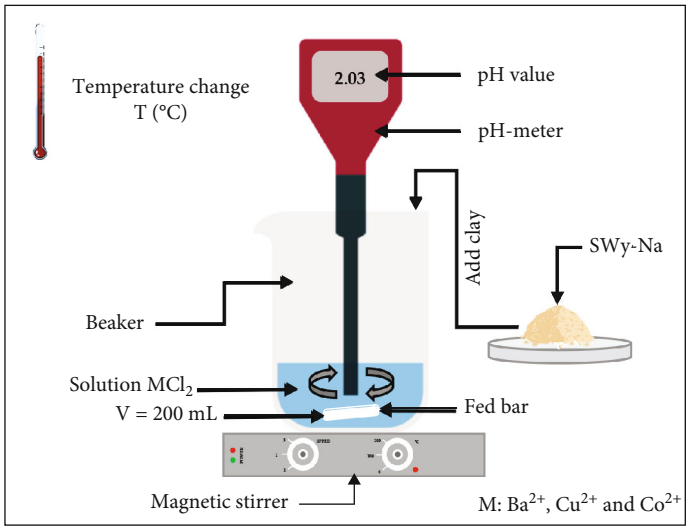

Figure 2: Experimental assembly of the 1st order coupling.

Table 1: Soil solution pH and temperatures of the coupling of the 1st order of the stresses.

Soil solution pH		Coupling of the 1st order		
		Temperature (°C)	Time (h)	V (mL)
Acid	3	50	24	200
	5	60		
Neutral	7	70		
Basic	9	80		
	11	90		

explored angular range. Indeed, the XRD profiles were recorded in the $2\theta^{\circ}$ range from 3.5 to 60 for all specimens. All records are made at room temperature under atmospheric pressure. XRD investigations were directed by the correlation between qualitative and quantitative analyses.

2.6.1. Semiquantitative XRD Analysis. The semiquantitative XRD investigation is carried out by determining, respectively, the observed homogeneity structure based on the 001 reflections shape, the experimental d_{001} basal spacing value, the calculated full width at the maximum half FWHM, the calculated crystallite size D, and the calculated rationality parameter ξ [98, 99]. This preliminary analysis

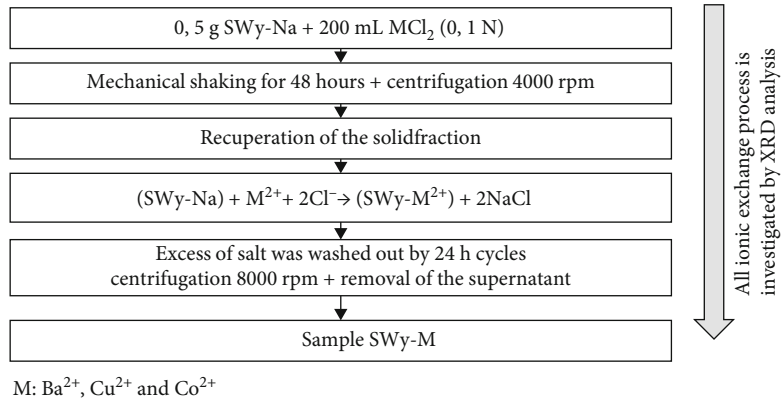

Figure 3: Experimental cation exchange protocol.

Table 2: The z atomic coordinates within the 2 : 1 layer framework along the c^* axis [42].

Atom type	O_1	O_2	O_3	O_4	O_5	O_6	OH_1	OH_2	Si_1	Si_2	Al
Number	2	1	2	2	1	2	1	1	2	2	2
Zn (Å)	0	0.20	2.25	4.31	6.26	6.59	1.98	4.28	0.59	6.04	3.43

remains insufficient to deeply identify interlamellar space (IS) contents, layer stacking mode at the crystallite size, the average layer number per stacking, the water molecule abundance and configuration, the saturation of the exchangeable intern and extern site, the hydration heterogeneities, the cause of the observed heterogeneity and the position, and the abundance of the exchangeable cation, and more.

2.6.2. XRD Profile Modeling: Theoretical Diffracted Intensity and Modeing Strategy. The modeling XRD approach is based on a matrix mathematical formalism developed by [42]. The expression of the intensity of the diffracted waves along the c^* axis is as follows:

$$I_{001}(2\theta) = L_p \mathrm{Spur}\left(\mathrm{Re}\,[\phi][W]\left\{[I] + 2\sum_{n}^{M-1}\left[\frac{M-n}{n}\right][Q]^n\right\}\right), \quad (2)$$

where Re means the real part of the final matrix, Spur is the sum of the diagonal terms of the real matrix, L_p is the Lorentz polarization factor, M is the number of layers per stack, $n = 1, \ldots, 1–M–1$, $[\Phi]$, is the matrix of the structural factor, $[I]$ is the unitary matrix, $[W]$ is the diagonal matrix of the proportions of the different types of layers, and $[Q]$ is the matrix representing the interference phenomena between the adjacent layers.

The modeling approach allowed us to identify the abundance of different layer types abundances (W_i), the type and the abundance of the mixed layer structure MLS, the stacking mode of different layer types, the average number M of layers per coherent scattering domain (CSD), and the IS water molecule distribution [78]. Within a CSD, layer stacking is described by a set of junction probabilities (P_{ij}). Briefly, the relationship between probabilities and W_i abundance of two different types of layers (i and j) can be summarized as follows: (i) the segregation tendency is given by $W_i < P_{ii}$ and $W_j < P_{jj}$, (ii) total demixing is obtained for $P_{ii} = P_{jj} = 1$, (iii) the regular tendency is obtained if $W_i < P_{ji} < 1$ and $W_j < P_{ij} < 1$, and (iv) finally, the boundary between the last distribution labeled chaotic/or random is obtained when $W_i = P_{ji} = P_{ii}$ and $W_j = P_{ij} = P_{jj}$ with $\Sigma W_i = 1$ and $\Sigma P_{ij} = 1$ [42, 100].

The modeling strategy consists of the theoretical reproduce of the experimental XRD profile initially from a homogeneous structure subsequently improved by adding other supplementary contributions. The existence of two mixed-layer structures (MLS) does not reflect the presence of two populations of particles physically present in the sample [48, 79, 101]. Therefore, layers with the same hydration state present in different MLS contributing to the diffracted intensity are assumed to have identical properties (chemical composition, layer thickness, and z-coordinates of atoms). The details of the XRD modeling approach are explained in detail in previous work of [41, 48, 78, 79, 101]. The atomic coordinates z in the 2 : 1 layer framework (octahedral layer sandwiched between two tetrahedral layers) are shown in Table 2. The z-coordinates of the IS content (exchangeable cation, molecules, etc.) are optimized, during the modeling process [66, 102], to improve the agreement R_{wp}:

$$R_{\mathrm{WP}} = \sqrt{\frac{\sum\left\{I(2\theta_i)_{\mathrm{exp}} - I(2\theta_i)_{\mathrm{calc}}\right\}^2}{\sum\left\{I(2\theta_i)_{\mathrm{exp}}\right\}^2}} \times 100\%, \quad (3)$$

where $I(2\theta_i)_{\mathrm{exp}}$ is the experimental diffracted intensity, and $I(2\theta_i)_{\mathrm{calc}}$ is the calculated ones.

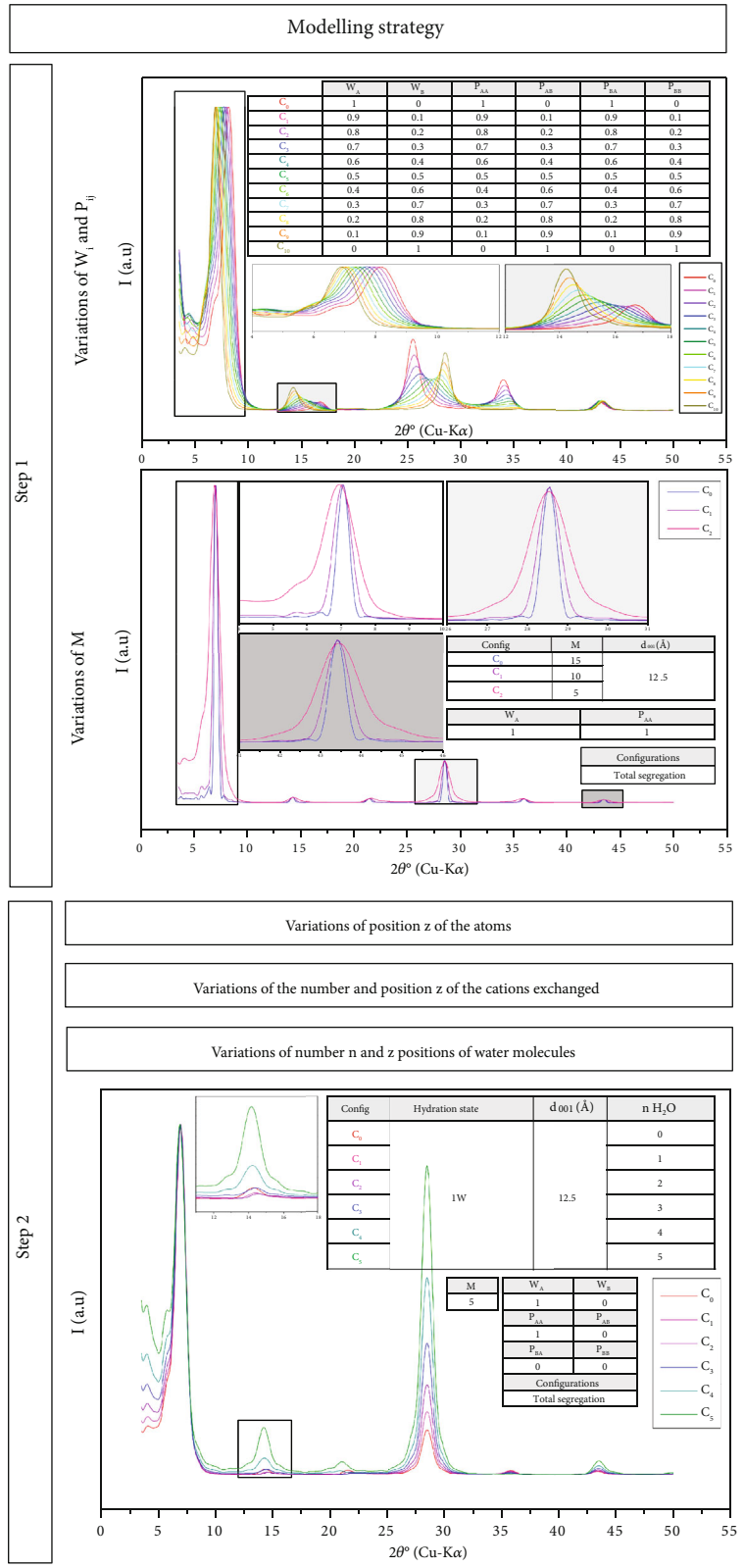

Figure 4: The main input structural parameter for the XRD modeling approach.

2.6.3. Modeling Strategy. The search for optimal structural parameters passes necessary through the determination of the shape function called "modulation function." It is related to the positions of the characteristic XRD reflections, by making the variations of the following parameters: (i) the W_i proportions of the different distances and the relative probabilities P_{ij} of succession law between layer type i and layer type j and (ii) the average layer number M per stack.

Table 3: Examples of half-cell structural formulas for raw montmorillonite SWy-2 and exchanged (SWy-2) with sodium and heavy metals at full saturation.

Samples	Structural half-cell formula
SWy-2	$(Si^{4+}_{3.96}, Al^{3+}_{0.04})\ (Al^{3+}_{1.53}, Fe^{3+}_{0.18}, Fe^{2+}_{0.045}, Mg^{2+}_{0.26}, Ti^{4+}_{0.01})\ O_{10}\ (OH)_2\ (Ca^{2+}_{0.07}, K^{+}_{0.01}, Na^{+}_{0.2})$
SWy-Na	$(Si^{4+}_{3.96}, Al^{3+}_{0.04})\ (Al^{3+}_{1.53}, Fe^{3+}_{0.18}, Fe^{2+}_{0.045}, Mg^{2+}_{0.26}, Ti^{4+}_{0.01})\ O_{10}\ (OH)_2\ (Na^{+}_{0.28})$
SWy-Co	$(Si^{4+}_{3.96}, Al^{3+}_{0.04})\ (Al^{3+}_{1.53}, Fe^{3+}_{0.18}, Fe^{2+}_{0.045}, Mg^{2+}_{0.26}, Ti^{4+}_{0.01})\ O_{10}\ (OH)_2\ (Co^{2+}_{0.14})$
SWy-Cu	$(Si^{4+}_{3.96}, Al^{3+}_{0.04})\ (Al^{3+}_{1.53}, Fe^{3+}_{0.18}, Fe^{2+}_{0.045}, Mg^{2+}_{0.26}, Ti^{4+}_{0.01})\ O_{10}\ (OH)_2\ (Cu^{2+}_{0.14})$
SWy-Ba	$(Si^{4+}_{3.96}, Al^{3+}_{0.04})\ (Al^{3+}_{1.53}, Fe^{3+}_{0.18}, Fe^{2+}_{0.045}, Mg^{2+}_{0.26}, Ti^{4+}_{0.01})\ O_{10}\ (OH)_2\ (Ba^{2+}_{0.14})$

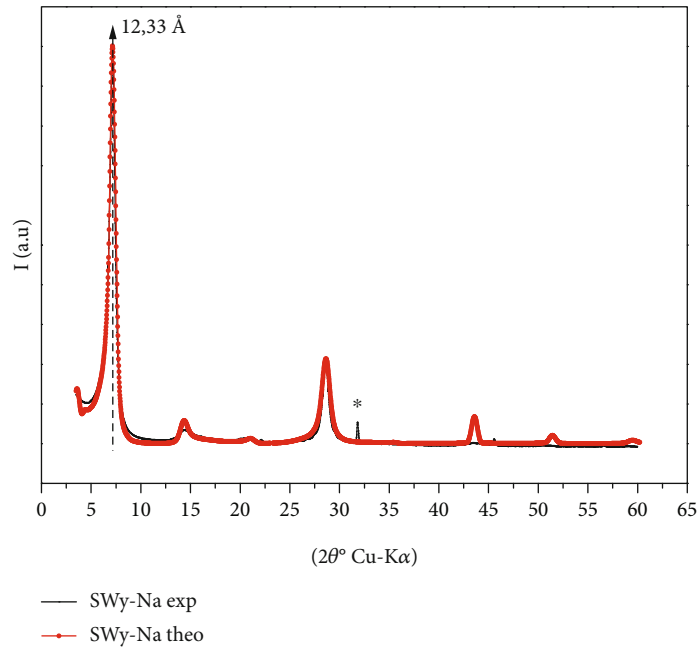

Figure 5: Best agreement between theoretical and experimental XRD profiles obtained in the case of SWy-Na. *Halite (NaCl).

Table 4: Qualitative XRD investigation in the case of the samples SWy-Na, SWy-Co, SWy-Cu, and SWy-Ba [47, 97].

Sample	$2\theta^\circ$	d_{001} (Å)	FWHM ($2\theta^\circ$)	D (Å)	ξ (Å)	Character
SWy-Na	7.16	12.33	0.74	18.77	0.062	Homogeneous
SWy-Co [47]	5.86	14.88	0.71	19.55	0.520	Interstratified
SWy-Cu [47]	7.14	12.36	0.61	22.77	0.100	Homogeneous
SWy-Ba [91]	5.91	14.94	1.55	08.96	0.970	Interstratified

Notes: $2\theta^\circ$: Bragg's angle; d_{001}: basal distance of the 1st reflection; D: average crystalline size; FWHM: full width at half maximum; ξ: rationality deviation parameters.

The agreement between theoretical and experimental profile is improved (decrease of R_{WP} value) by some adjustment attributed to the following parameters: (i) the z position of the layer atom composition along the c^* axis, (ii) the number and position z of the exchangeable cations, and (iii) the abundance and the configuration (their z positions following the normal at the sheet plane [82, 99, 103, 104] of the interlayer water molecules). A brief modeling strategy summary is reported in Figure 4.

2.7. Thermal Analysis: Thermogravimetry/Differential Thermal Analysis (TG/DTA). The hydration properties are very sensitive to the amount of water molecule which is identified by TG-DTA thermal analyses coupled with the "Labsys TG" model. All TG-DTA records are realized at variable temperatures from 0 to 500°C at a speed of 5°C/min. The used gas stream is argon. Approximately 10 mg of sample was used in platinum pans in each analysis. The determination of nH_2O necessarily depends on the results drawn from the TG-DTA curves followed by a theoretical calculation via modeling. After having optimized the theoretical XRD models, a structural formula per half unit cell can be determined by taking into account the weighting of each MLS and then of each layer population and its specific weighting as well as the average number of layers per crystallite (Table 3). Subsequently, the molar mass of the obtained results is calculated. The number of nH_2O (abundance) is estimated according to the following parameters: the initial

Table 5: Optimum structural parameters used for modeling XRD profiles in the case of baseline samples [47, 97].

Sample	% MLS	d_{001}	nH_2O	W_A	P_{AA}	S_M	M	R_{WP} (%)
SWy-Na	80	10.5	0	0.80	0.85	R_{1-seg}	10	2.27
	20	12.5	2					
SWy-Co [47]	16	12.4	1.1	0.16	0.30	R_{1-seg}	8	4.25
	84	15.2	1.9					
SWy-Cu [47]	95	12.4	1.1	0.95	0.05	R_{1-seg}	8	3.82
	05	15.2	1.9					
SWy-Ba [91]	64	12.4	1.1	0.15	0.15	R_0	8	3.77
		15.2	1.9					
	36	12.4	1.1	0.65	0.77	R_{1-seg}		
		15.2	2.0					

Notes: d_{001}: interlamellar distance; nH_2O: number of water molecules per half-cell; zH_2O: position of the molecules along the c^* axis of the H_2O molecule is attached to 9.6 Å for hydration states 1 W. The position of the exchangeable cations per half-cell calculated along the axis c^* is fixed à 9.6 Å for hydration states 1 W [41]. M: average number of sheets per stack; S_M: layer stacking mode; R_0: maximum order; R_1: random stacking; R_{1-X}, associated stacking (segregation-partial order); C: characters; Ho: homogeneous; He: heterogeneous; R_{WP}: confidence factor.

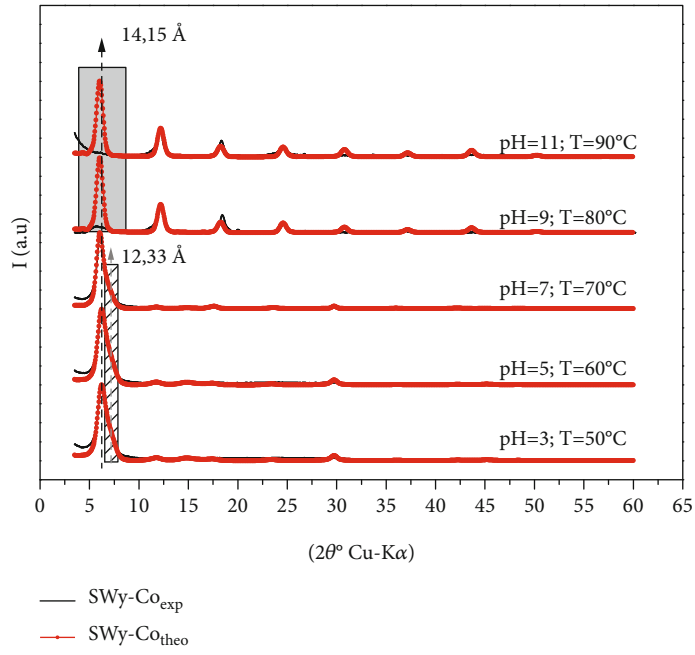

Figure 6: Best agreement between theoretical and experimental XRD profiles obtained in the case of SWy-Co.

mass $m_{initial}$ of the sample before analysis, the variation in sample mass Δm, the average number of layers M, and the number of moles n (deduced from masse molar).

2.8. Adsorption Analysis and Porosity Investigation. This study uses BET analysis in order to gain insight in particular surface area (SA) estimation in the case of porous materials, yielding knowledge in the effects of porosity fate and particle size evolution versus constraint strength [41, 105, 106]. This goal is achieved by multilayer nitrogen adsorption isotherm variation (performed at 77 K) versus relative pressure (P /P0~0.95). This task is fully automated manipulating Quantachrome NOVA 2000e series volumetric gas adsorption instrument. BJH analysis is employed to define pore area and specific pore volume by means of adsorption and desorption procedures. Also, the pore size distribution (PSD) was identified assuming several pores shape approximations. The adsorbed nitrogen and oxygen were eliminated under reduced (vacuum) pressure at 100°C for 8 h before measuring SA and PSD [107–110].

3. Results and Discussion

3.1. Semiquantitative XRD Investigation of the Baseline Samples. The experimental XRD profile of the starting SWy-Na complex (Figure 5) shows three characteristic reflections ($n = 1$, 2, and 4). The first reflection (001) is located at $2\theta = 7.16°$ ($d_{001} = 12.33$ Å) probably indicating a hydration 1 W state (Table 4). By calculating the FWHM and ξ parameter value, the homogeneous observed character is confirmed [111, 112]. This result is consistent with the results of [48] on the same sample. Na-rich montmorillonite

Table 6: Qualitative XRD investigation in the case of the samples SWy-Co SWy-Cu and SWy-Ba.

Samples		$2\theta^{\circ}$	d_{001} (Å)	FWHM ($2\theta^{\circ}$)	D (Å)	ξ (Å)	Characters
SWy-Co	pH = 3; T = 50°C	06.22	14.20	1.27	10.93	0.563	Interstratified
	pH = 5; T = 60°C	06.24	14.15	1.18	11.77	0.653	
	pH = 7; T = 70°C	06.09	14.50	1.00	13.89	0.406	
	pH = 9; T = 80°C	06.07	14.55	1.93	07.19	0.109	
	pH = 11; T = 90°C	*	*	*	*	*	
SWy-Cu	pH = 3; T = 50°C	07.16	12.34	0.61	22.77	0.016	Homogeneous
	pH = 5; T = 60°C	07.03	12.57	0.71	19.57	0.096	
	pH = 7; T = 70°C	07.08	12.48	1.74	07.98	0.114	
	pH = 9; T = 80°C	07.06	12.51	1.97	07.05	0.207	Interstratified
	pH = 11; T = 90°C	07.00	12.62	2.14	06.49	0.270	
SWy-Ba	pH = 3; T = 50°C	07.18	12.30	0.70	19.85	0.055	Homogeneous
	pH = 5; T = 60°C	07.14	12.37	1.30	10.69	0.013	Interstratified
	pH = 7; T = 70°C	07.20	12.27	0.55	25.26	0.091	
	pH = 9; T = 80°C	07.18	12.30	0.68	20.43	0.216	Homogeneous
	pH = 11; T = 90°C	07.35	12.02	0.57	24.38	0.064	

Notes:*absence of the 001 reflection.

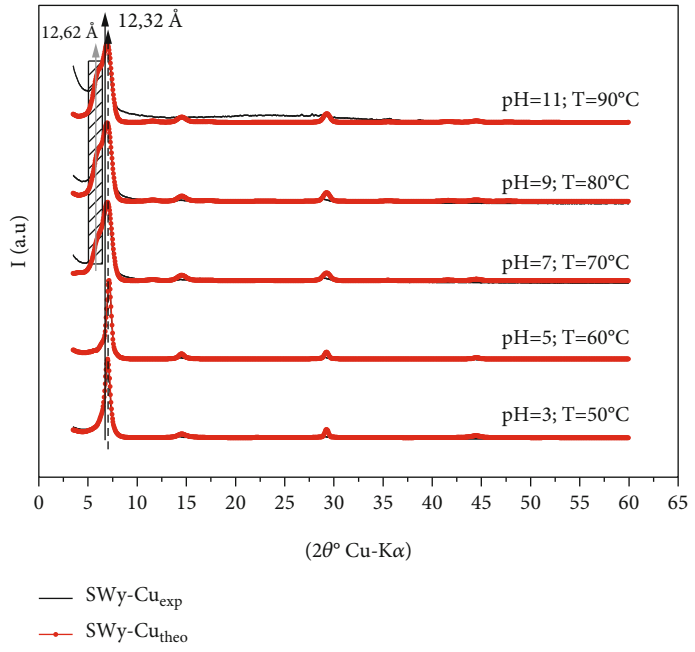

Figure 7: Best agreement between theoretical and experimental XRD profiles obtained in the case of SWy-Cu.

(SWy-Na) has been studied extensively before since it is considered a reference sample [5–7, 41, 48, 78–79, 89, 113]. At this level, our goal is to refine the obtained literature results related to the SWy-Na sample. For the SWy-Cu, SWy-Co, and SWy-Ba samples, qualitative and quantitative XRD results extracted from the same authors earlier works [47, 97] are used (Tables 4 and 5).

3.2. Modeling of XRD Profiles in the Case of SWy-Na Sample. The mixed layer structure (MLS) used to achieve the best agreement between the experimental and calculated XRD model (Figure 5) shows an heterogeneous hydration character that results in the coexistence of two types of layers (0 W and 1 W) with a strong dominance for the 1 W phase at about 80%. This opposes the obtained qualitative description.

Indeed, the distribution of IS water molecules has respected the previous work [5, 6, 48, 88, 101] with a water sheet located in the middle of the IS for 1 W phase and the absence of water in the IS for the dehydrated state 0 W. Regardless of the type of hydration state, the exchangeable cations Na (per half-cell unit) are positioned in the center of the IS along the c^* axis respecting the configuration of

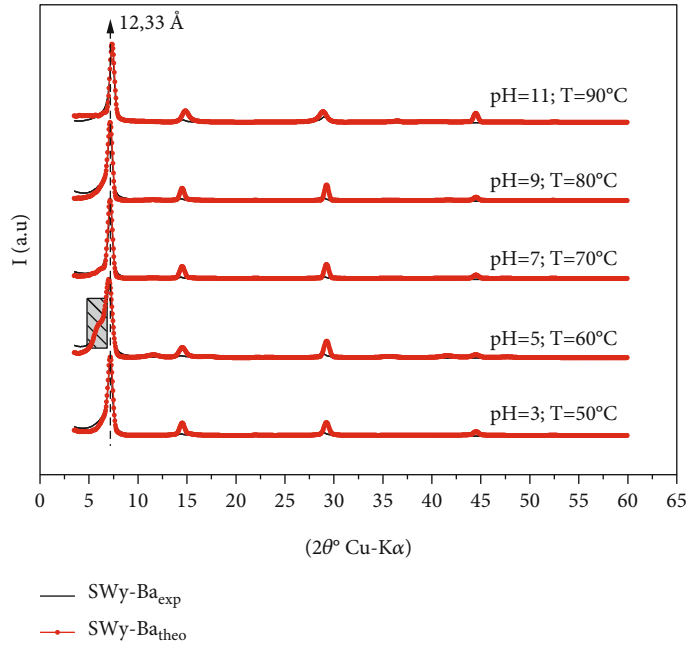

Figure 8: Best agreement between theoretical and experimental XRD profiles obtained in the case of SWy-Ba.

the data provided by the literature [5, 48]. The average number of layers per crystallite M is equal to 10. The confidence factor R_{WP} is very low (2.27%), which reflects the high quality of fitting. The structural parameters are summarized in Table 5.

3.3. Semiquantitative Description of XRD Analysis after Applying First-Order Coupling Stress

3.3.1. Case of the SWy-Co Sample. The experimental XRD results for the SWy-Co samples obtained are shown in Figure 6. For the first three constraint coupling levels (pH = 3; T = 50°C ⟶ pH = 7; T = 70°C), there is an asymmetry for the main 001 reflections located at 6.1 in 2θ° with d_{001} ~ 14.5 Å synonymous of a minor 2 W hydration state presence attributed to the Co^{2+} cation in IS. Also, a shoulder towards the wide angles around in 7.2° in 2θ (d_{001} ~ 12.3 Å) attributed to the existence of the sodium residue resulting from the starting sample. Generally, the observed asymmetric 001 reflections indicates the coexistence of several hydration states within the crystallite and/or a partial cation exchange process. The values of the FWHM and ξ parameters confirms this idea (Table 6).

In Table 6, for the rest of the samples, a different hydration behavior was observed. The diffracted intensity ratio I_{001}/I_{002}, I_{001}/I_{003}, and I_{001}/I_{004} of the complex studied under (pH = 9, T = 80°C/pH = 11, T = 90°C) decreases if compared with the three first studied samples. Also, a drastic decrease in the 001-reflection intensity is observed in both samples and which probably indicates a bottom transformation that affected the structure when increasing constraints strength. This strange structural behavior finds an explanation by the effect of the increase in temperature and the basic aspect of the soil solution pH on the cohesion energy between layers and even destruction of the chemical bonds within octahedral and tetrahedral sheet forming the layer. The main structure is affected and an elevated layer's exfoliation trends within the crystallites favoring a total transformation of the original 2 : 1 phase to a 1 : 1 clay structure that was established. The raised value of the 002-reflection intensity and the absence of the 001 line can be interpreted in this case by the beginning of a great structural transformation. This remains to be proven by quantitative XRD analysis and by studying the porosity evolution of these two samples.

3.3.2. Case of the SWy-Cu Sample. The experimental XRD models, in the case of SWy-Cu, obtained by varying the external constraint strength are summarized in Figure 7. For the first two constraints of the coupling value (pH = 3; T = 50°C and pH = 5; T = 60°C), the experimental XRD models are almost identical with a low FWHM value (Table 6) indicating probably either the coexistence, within the stacks, of several hydration states [77] or an unfinished (partial) cation exchange, knowing that Cu^{2+} cation is indistinguishable from the starting sodium by simple XRD analysis at room conditions from the starting sodium cation [47]. All qualitative parameters are summarized in Table 6. For the rest of the complexes (pH = 7; T = 70°C ⟶ pH = 11; T = 90°C), a stack towards the small angles (5.9° ⟶ 15 Å) appeared and ascribed to the material response to the applied stress. Indeed, a beginning of 2 W transition, without a real domination, is confirmed by increasing the coupling constraint intensity. It remains to be noted that the higher-order peaks have a relatively low intensity regardless surrounding environment change and from soil solution pH value = 7 and temperature T = 70°C, an abrupt structural change is observed.

3.3.3. Case of the SWy-Ba Sample. The experimental XRD profiles of SWy-Ba sample are reported in Figure 8. An

Table 7: Structural parameters of SWy-Co, SWy-Cu, and SWy-Ba.

Samples		% MLS	xW-echa.cat	d_{001}	nH_2O	W_A	P_{AA}	S_M	M	M_{tot}	R_{WP}
SWy-Co	pH = 3; T = 50°C	16.68	1 W-Na	12.2	0.0442	1	1	R_0	05		
		83.28	1 W-Na	12.2	0.0346	0.40	0.55	R_{1-seg}	10	9	3.61
			2 W-Co	15.2	0.0259						
					0.0259						
	pH = 5; T = 60°C	16.70	1 W-Na	12.2	0.0322	1	1	R_0	05		
		83.30	1 W-Na	12.2	0.0252	0.40	0.55	R_{1-seg}	10	9	3.79
			2 W-Co	15.2	0.0189						
					0.0189						
	pH = 7; T = 70°C	35	1 W-Na	12.2	0.0230	0.35	0.63	R_{1-seg}	08	8	3.42
		65	2 W-Co	15.2	0.0300						
					0.0300						
	pH = 9; T = 80°C	40	1 W-Na	12.2	0.0200	0.40	0.40	R_0	07	7	7.45
		60	2 W-Co	15.2	0.0243						
					0.0243						
	pH = 11; T = 90°C	40	1 W-Na	12.2	0.0101	0.40	0.40	R_0	07	7	9.12
		60	2 W-Co	15.2	0.0113						
					0.0113						
SWy-Cu	pH = 3; T = 50°C	81.23	1 W-Na	12.2	0.1166	0.95	0.95	R_0	14	12	3.84
			2 W-Cu	15.2	0.0031						
					0.0031						
		18.77	1 W-Na	12.2	0.0333	0.95	0.95	R_0	04		
			2 W-Cu	15.2	0.0009						
					0.0009						
	pH = 5; T = 60°C	84.20	1 W-Na	12.2	0.0797	0.85	0.86	R_{1-seg}	14	12	3.56
			2 W-Cu	15.2	0.0070						
					0.0070						
		15.80	1 W-Na	12.2	0.0228	0.85	0.86	R_{1-seg}	04		
			2 W-Cu	15.2	0.0020						
					0.0020						
	pH = 7; T = 70°C	75	1 W-Na	12.2	0.0410	0.75	0.90	R_{1-seg}	10	10	4.92
		25	2 W-Cu	15.2	0.0068						
					0.0068						
	pH = 9; T = 80°C	70	1 W-Na	12.2	0.0250	0.70	0.87	R_{1-seg}	08	8	6.04
		30	2 W-Cu	15.2	0.0148						
					0.0148						
	pH = 11; T = 90°C	70	1 W-Na	12.2	0.0284	0.70	0.87	R_{1-seg}	08	8	7.73
		30	2 W-Cu	15.2	0.0061						
					0.0061						
SWy-Ba	pH = 3; T = 50°C	72.17	1 W-Na	12.2	0.1001	1	1	R_0	12		
		27.83	1 W-Na	12.2	0.0446	0.90	0.89	$R_{1-p.ord}$	06	10	5.41
			2 W-Ba	15.2	0.0045						
					0.0045						
	pH = 5; T = 60°C	84	1 W-Na	12.2	0.0978	0.84	0.91	R_{1-seg}	10	10	5.96
		16	2 W-Ba	15.2	0.0093						
					0.0093						
	pH = 7; T = 70°C	95	1 W-Na	12.2	0.0905	0.95	0.97	R_{1-seg}	12	12	5.22
		05	2 W-Ba	15.2	0.0045						
					0.0045						

Table 7: Continued.

Samples	% MLS	xW-echa.cat	d_{001}	nH_2O	W_A	P_{AA}	S_M	M	M_{tot}	R_{WP}
pH = 9; T = 80°C	65.75	1 W-Na	12.2	0.0611	1	1	R_0	13	13	5.37
	34.25	1 W-Na	12.2	0.0202	0.80	0.85	R_{1-seg}	13		
		2 W-Ba	15.2	0.0025						
				0.0025						
pH = 11; T = 90°C	15	0 W-Na	10.2	0.0000	0.85	0.83	$R_{1-p.ord}$	13	13	5.16
	85	1 W-Ba	12.2	0.0750						

Notes: xW-echa.cat: layer type and associated exchangeable cation; d_{001}: interlamellar distance; nH_2O: number of water molecules per half-cell; zH_2O: position of the molecules along the c^* axis of the H_2O molecule is attached to 9.6 Å and 11.3 Å–13.9 Å for hydration states 1 W and 2 W, respectively. The position of the exchangeable cations per half-cell calculated along the axis c^* is fixed with 9.60 Å and 12.25 Å for hydration states 1 W and 2 W [41]; n-echa.cat: number of exchangeable cations per half-cell is set to 0.28 (for the cation Na^+) and at 0.14 (for bivalent metal cations), indicating complete saturation of cation exchange capacity (CEC); M: average number of sheets per stack; M_{tot}, total average number of sheets per stack; S_M: layer stacking mode; R_0: maximum order; R_1: random stacking; R_{1-X}: associated stacking (segregation-partial order); C: characters; Ho: homogeneous; He: heterogeneous; R_{WP}: confidence factor.

Table 8: Results from TG/DTA analyses in the case of samples SWy-Co, SWy-Cu, and SWy-Ba.

Samples		$m_{initial}$ (mg)	Δm (mg)
SWy-Co	pH = 3; T = 50°C	15.90	09.974
	pH = 5; T = 60°C	16.60	13.387
	pH = 7; T = 70°C	06.80	01.820
	pH = 9; T = 80°C	17.10	11.074
	pH = 11; T = 90°C	12.30	08.605
SWy-Cu	pH = 3; T = 50°C	17.50	12.975
	pH = 5; T = 60°C	17.40	14.246
	pH = 7; T = 70°C	15.70	12.836
	pH = 9; T = 80°C	11.30	06.972
	pH = 11; T = 90°C	14.00	10.848
SWy-Ba	pH = 3; T = 50°C	15.00	06.773
	pH = 5; T = 60°C	23.60	19.570
	pH = 7; T = 70°C	15.00	06.731
	pH = 9; T = 80°C	15.40	03.501
	pH = 11; T = 90°C	19.10	12.462

Notes: $m_{initial}$: initial mass of the samples before analysis; Δm: change in mass during analysis.

Table 9: Radius and ionic potential of some cations [110].

Cations	Ionic potential (eV)	Ionic radius (Å)
Na^+	1.05	0.95
Ba^{2+}	1.48	1.35
Cu^{2+}	2.74	0.73
Co^{2+}	3.08	0.65

intense 001 reflection situated at 7.2° (2θ) (d_{001} ~ 12.3 Å) indicating a 1 W hydration state dominates all sample. This probably reflects the existence of a Na^+ residue originating from the starting sample or from added NaOH solution used to balance the pH solution. This opposes the earlier results [41, 97] on cation exchange in the case of Ba^{2+} which demonstrate a 2 W hydration state behavior.

For pH = 5/T = 60°C, the XRD profile shows a shoulder towards the low angles (5.8° ⟶ d_{001} = 15.23 Å) with an increase in the FWHM and ξ parameter value indicating the 2 W hydration state transition beginning. Also, it can be interpreted by the coexistence, within the stacks, of several states of hydration [77] or an unfinished (partial) cation exchange knowing that the barium hydrate baseline to two layers of water 2 W (15 Å). All qualitatively estimated parameters are summarized in Table 6.

3.4. XRD Modeling Profiles after Applying First-Order Coupling Stress

3.4.1. Case of the SWy-Co Samples. The qualitative XRD analysis suggested heterogeneous hydration behavior for SWy-Co samples, regardless of the strength of the stresses applied. This interstratification has been approved by the 001 reflection modeling approach which assumes the coexistence of two different hydration states (e.g., 1 W and 2 W). To improve the agreement between the calculated and experimental models (Figure 6) and for each constraint strength from pH = 5/T = 60°C towards pH = 11/T = 90°C, the proposed MLS is theoretically decomposed into two layer populations type (i.e., 1 W: d_{001} ~ 12.2 Å and 2 W: d_{001} ~ 15.2 Å) stacked according to specific succession probability laws. The structural parameters associated with this modeling approach are summarized in Table 7. The proposed MLS is obtained by weighted layer populations that are tolerated to have an identical chemical composition, identical layer thickness, and identical z-atoms coordinates [40, 48]. The CEC of the results is partially saturated by the Na^+ and Co^{2+} cations since, under ambient conditions, sodium always has a hydration state of 1 W [41, 48], and cobalt has a hydration state of 2 W.

The theoretical decomposition of the SWy-Co sample, (pH = 11; T = 90°C) which has undergone fundamental changes in its basic structure, can be followed by two major hypotheses:

The 1st consists in considering that it is still a T-O-T type structure despite the absence of the main 001 reflection which must be positioned around 6.1° (2θ) (d_{001} ~ 14.5 Å) and can be attenuated (is no longer sensitive to X-rays during diffractogram recordings) following the increase in the

Table 10: Evolution of the nH_2O amounts versus constraint strength for samples SWy-Co, SWy-Cu, and SWy-Ba.

Samples		Phases	Saturation		m_{molar} (g/mol)	M	nH_2O
			% Na^+	% M^{2+}			
SWy-Co	pH = 3; T = 50°C	Phase 1	100	0	370.864	05	0.0442
		Phase 2	16.68	83.28	379.250	10	0.0865
	pH = 5; T = 60°C	Phase 1	100	0	370.864	05	0.0322
		Phase 2	16.70	83.30	379.248	10	0.0630
	pH = 7; T = 70°C	Ø	35	65	377.406	08	0.0833
	pH = 9; T = 80°C	Ø	30	70	377.909	07	0.0686
	pH = 11; T = 90°C	Ø	30	70	377.909	07	0.0327
SWy-Cu	pH = 3; T = 50°C	Phase 1	95	05	371.432	14	0.1228
		Phase 2	95	05	371.432	04	0.0351
	pH = 5; T = 60°C	Phase 1	85	15	372.568	14	0.0937
		Phase 2	85	15	372.568	04	0.0268
	pH = 7; T = 70°C	Ø	75	25	373.703	10	0.0546
	pH = 9; T = 80°C	Ø	70	30	374.271	08	0.0358
	pH = 11; T = 90°C	Ø	70	30	374.271	08	0.0406
SWy-Ba	pH = 3; T = 50°C	Phase 1	100	00	370.864	12	0.1001
		Phase 2	90	00	374.066	06	0.0496
	pH = 5; T = 60°C	Ø	84	16	375.988	10	0.1164
	pH = 7; T = 70°C	Ø	95	05	372.465	12	0.0995
	pH = 9; T = 80°C	Phase 1	100	00	370.864	13	0.0611
		Phase 2	80	20	377.267	13	0.0252
	pH = 11; T = 90°C	Ø	15	85	398.076	13	0.0750

Notes: phases: modeling phase of each sample; Ø: absence of phases; m_{molar}: molar mass of the sample related to each phase; 4: average number of layers per stack; nH_2O: number of water molecules per half-cell bound to each phase.

applied stress strength. In this case, a theoretical model based on the heterogeneous mixed 1 W/2 W structure with a major domination for the phase 2 W was adopted with very low average layer number per crystallite. This hypothesis can be practically verified for the good agreement towards higher diffraction orders.

The 2nd considers that the basic clay structure has been strictly modified following the coupled increase in temperature T and the soil solution pH during the cation exchange process. This supposition is justified through the destruction of chemical bonds within the crystallite and/or which give rise to a new structure derived from smectite. This result, despite its originality, agrees with the work of [108, 109] which focuses on the hydrothermal synthesis of zeolite from clay minerals by controlling the pH effect on the synthesis process. Hence, the transition from a T-O-T phyllosilicate type (montmorillonite) to another kaolinite T-O phyllosilicate type is probabilistic, knowing that kaolinite has a dioctahedral structure [114–116]. Its structural half-cell formula is defined by (Si_4 Al_4 O_{10} $(OH)_8$), whose basal distance d_{001} is of the order of 7 Å [117–119] with a closed IS accompanied by the absence of isomorphic substitutions (not CC in the middle of IS). For this hypothesis (Figure 6), we consider that the first reflection (in the 1st hypothesis was considered as 2nd reflection 002) is positioned around 12° (2θ) (d_{001}~7 Å) from where the second reflection is necessarily positioned around 24° (2θ) (Table 7). For this hypothesis, we note the presence of a relatively intense reflection around 18° (2θ). A rational reflection position is obtained for the three reflections order (12° ⟶ 18° ⟶ 24°). Also, the exchangeable cation has no place in this configuration, which even calls into question the cation exchange process. Therefore, the first supposition seems more scientifically logical. The 1st hypothesis has been adopted in the rest of the calculations. It remains to be noted that the quality of the fitting is controlled by the R_{WP} parameter.

3.4.2. Case of the SWy-Cu Samples. The best agreement between theoretical and experimental XRD patterns (Figure 7) of the SWy-Cu samples is obtained using an interstratified structure of two MLS comprising various relative layers proportions with different hydration states (Table 7). This variability confirms the heterogeneous hydration character and the intermediate 1 W-2 W hydration phase observed regardless of the intensity of the applied constraints. In detail, a minor contribution of the 2 W phase increases from 5% to 30% by increasing the intensity of the external applied stress (pH = 3; T = 50°C ⟶ pH = 11; T = 90°C). Indeed, the 2 W hydration phase implemented in the theoretical model is necessarily attributed to the layer fraction whose CEC is saturated by Cu^{2+}. This weighting fluctuation is evidence of an incomplete cation exchange process (d_{001} < 15 Å). On the other hand, the dominance of

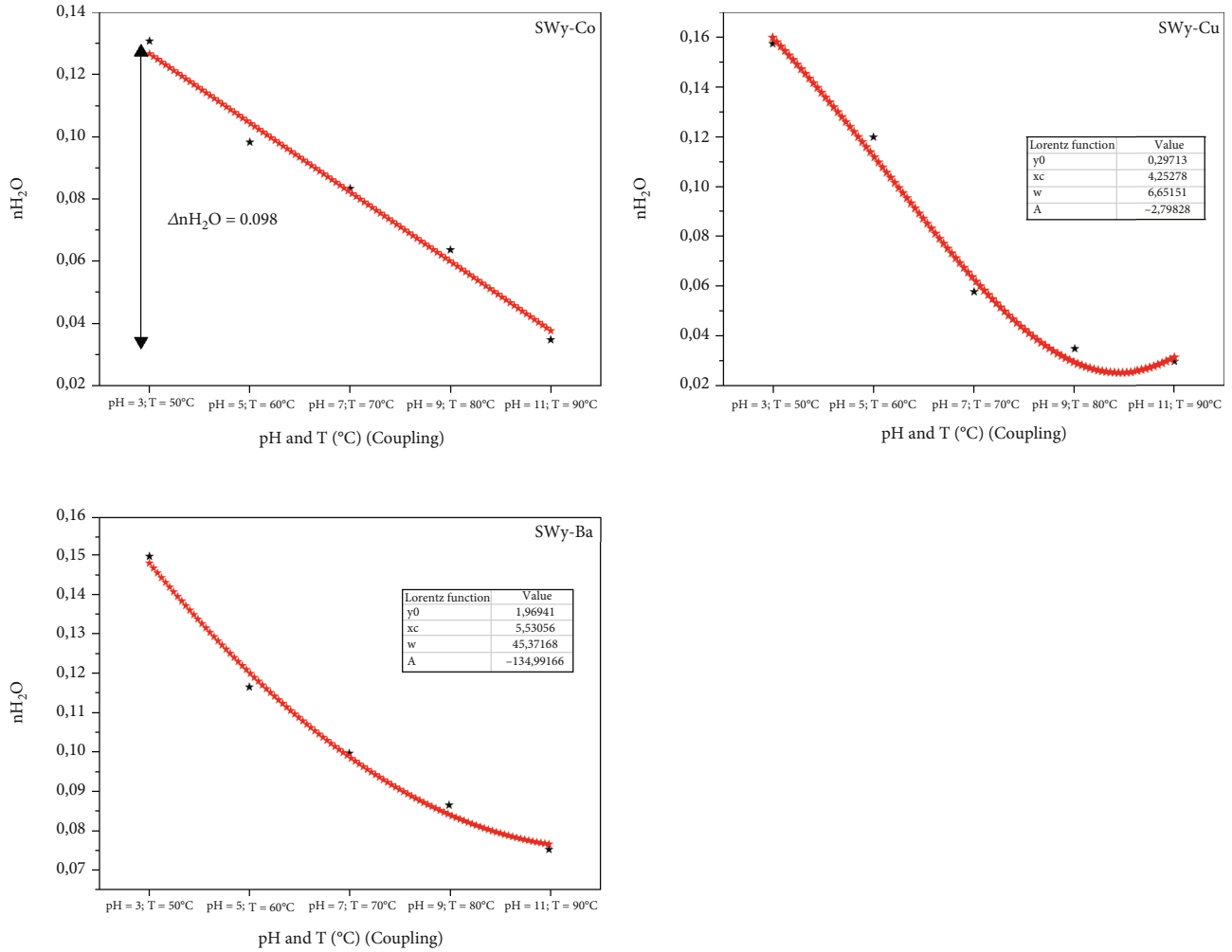

FIGURE 9: nH_2O abundance fluctuation as a function of stress strength for SWy-Co, SWy-Cu, and SWy-Ba samples (black scatter). Red scatter: the used linear and Lorentz fit function, respectively.

1 W layer hydration phase is interpreted by the existence of a fraction (quite large) regardless of the applied constraints applied. This contribution is attributed to the sodium residues from the starting sample (SWy-Na).

The agreements obtained between the experimental and theoretical profiles (R_{WP} ~ 3% to 8%) are generally acceptable (< 10%), despite the misfit observed after widening the peaks around 14° and 28° (2θ). In fact, this disagreement can be broken down into a good reflection position agreement and a disagreement of diffracted intensity related to the input fluctuation of the distribution and abundance of water molecules in the IS. This disagreement led us to explore wide-angle areas, later to establish a possible link between CEC saturation and the degree of hydration heterogeneity.

The logical increase of the R_{WP} factor in the case of SWy-Cu sample reflects the increase in the heterogeneity's degree defined, respectively, by an asymmetry of the first 001 reflections, the high FWHM value, and the ξ rationality parameter. Theoretically, this result is related to the variability of possible MLS configurations allowing a good fit of the 001 reflection. The exploitation of the W_A, P_{AA}, M, and R_{WP} values allowed us to characterize a specific distribution of the n normalized layers within the crystallites according to the generated stacking modes and the contribution of each phase. This statistical representation of the layer can help to understand the CEC sensitivity fluctuation (of the starting sample) following the variation in the temperature T and pH during the cation exchange process.

3.4.3. Case of the SWy-Ba Samples. For SWy-Ba samples, the best agreements between theoretical and experimental models are shown in Figure 8. The main structural parameters used to achieve a good fit are summarized in Table 7. For each model, several types of layers with variable stacking mode are used to improve the agreement obtained between the experimental and calculated models. This MLS is composed by several layers of type populations depending on the hydration state (0 W, 1 W, and 2 W) whose basal distance d_{001} is equal to 10.2 Å, 12.2 Å, and 15.2 Å, respectively. This variability confirms the heterogeneous hydration character observed by qualitative XRD analysis for the entire

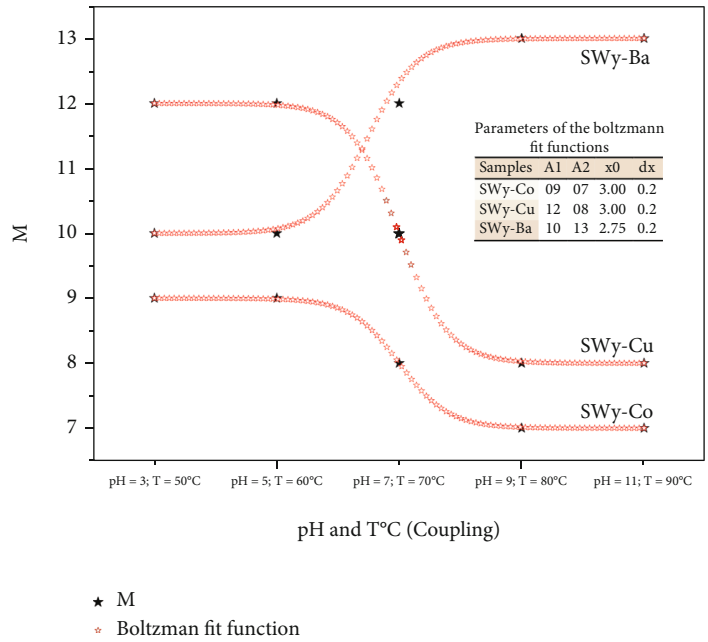

FIGURE 10: Average number of layers M evolution versus constraint strength in the case of SWy-Co, SWy-Cu, and SWy-Ba samples (black scatter). Red scatter: the used Boltzmann fit.

SWy-Ba series (pH = 3; $T = 50°C \longrightarrow$ pH = 11; $T = 90°C$) with a major dominance for the 1 W hydration phase saturated by Na^+ cation assigned to the starting sample. In addition, the 2 W phases are assigned to the fraction whose CEC is saturated by Ba^{2+} cation [41]. More specifically, for the first four samples from pH = 3/$T = 50°C$ towards pH = 9 /$T = 80°C$, an omnipresent minor contribution of the 2 W phase which does not exceed 16% is noted and which is evidence of the incomplete cation exchange process. In addition, the quite important dominance of the 1 W hydration phase (about 90%) is noted. The last sample (pH = 11; $T = 90°C$) has another intermediate phase 0 W/1 W which explain the observed decrease in basal distance probably resulting in the shrinkage of IS as a result of the temperature increase. The quality agreements obtained between the theoretical and experimental profiles are in average of ~5% which is generally acceptable.

3.5. Evolution of the Water Molecule Abundances versus Coupling Constraint Strength

3.5.1. Evolution of the nH_2O Amounts versus Constraint Strength. The delicate theoretical determination of nH_2O amounts for each studied sample is deduced from the results of thermogravimetry/differential thermal analysis (TG/DTA) (Figure S1) and summarized in Table 8.

Regardless of the sample type, the hydration state is governed by the cationic nature, the layer charge value, and the layer charge location [5–7, 107, 108, 120–122]. All samples studied belongs to the Wyoming montmorillonite specimen characterized by the same layer charge and the charge location value. The nature of the exchangeable cations and the external stresses applied to the cation exchange process (first-order coupling constraint) is at the origin of these specific water molecule amounts fluctuations. The water affinity of the exchangeable cation is related to the ionic potential which is defined by the ratio of the valence of the cation to its ionic radius [110] (Table 9). As this potential increases, the cation's affinity for water also increases. Indeed, bivalent cations such as cobalt (Co^{2+}), copper (Cu^{2+}), and barium (Ba^{2+}) have a high affinity of water translated by a 2 W hydration state [6, 7]. Unlike monovalent cations like sodium (Na^+), having a low affinity for water mainly generates monohydrated states 1 W.

Based on the quantitative XRD analysis, a discretization of the content of the IS is carried out. Indeed, the evolution of nH_2O molecules per half-cell, relative to the constraint strength, is described by Table 10 and represented in Figure 9. For all series, a decrease in the water molecules amounts as a function of the increase in temperature and soil solution pH.

In the case of SWy-Co sample (Figure 9), there is an overall linear decrease in the number of water molecules as a function of the increase applied stresses intensity (pH = 3 ; $T = 50°C \longrightarrow$ pH = 11; $T = 90°C$). Using a linear regression approach, a mathematical equation was developed. The behavior and evolution of the nH_2O abundance fluctuation re described by the following function:

$$y = 0.14888 - 0.02226.x, \tag{4}$$

where y is the nH_2O abundance fluctuation, and x is the applied stress intensity.

In the case of SWy-Cu and SWy-Ba samples (Figure 9), there is a nonlinear water molecule amount decrease unlike SWy-Co as a function of the increase in external stresses

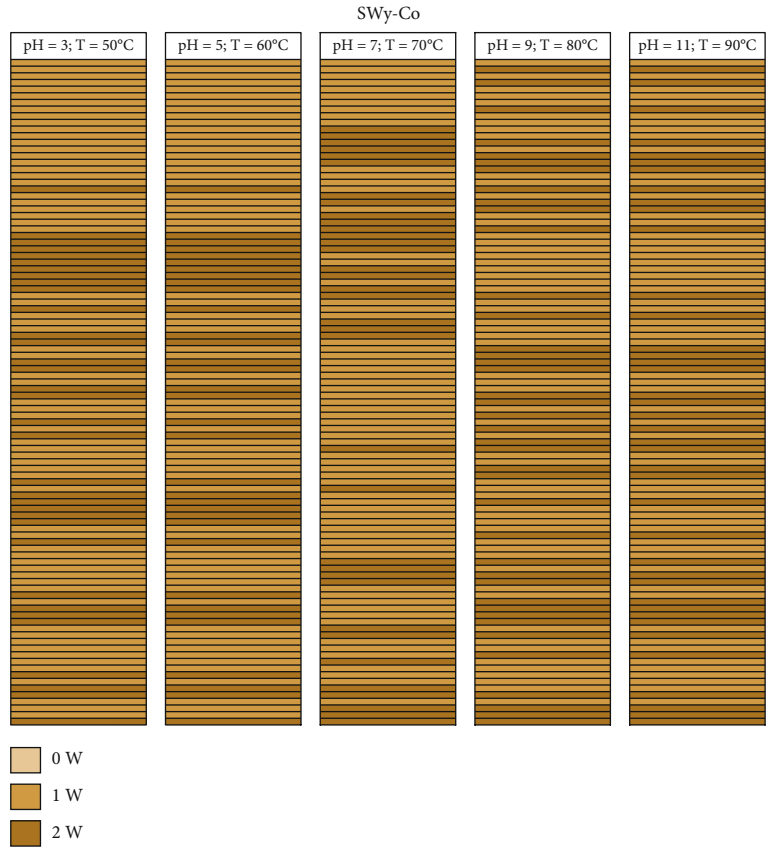

(a)

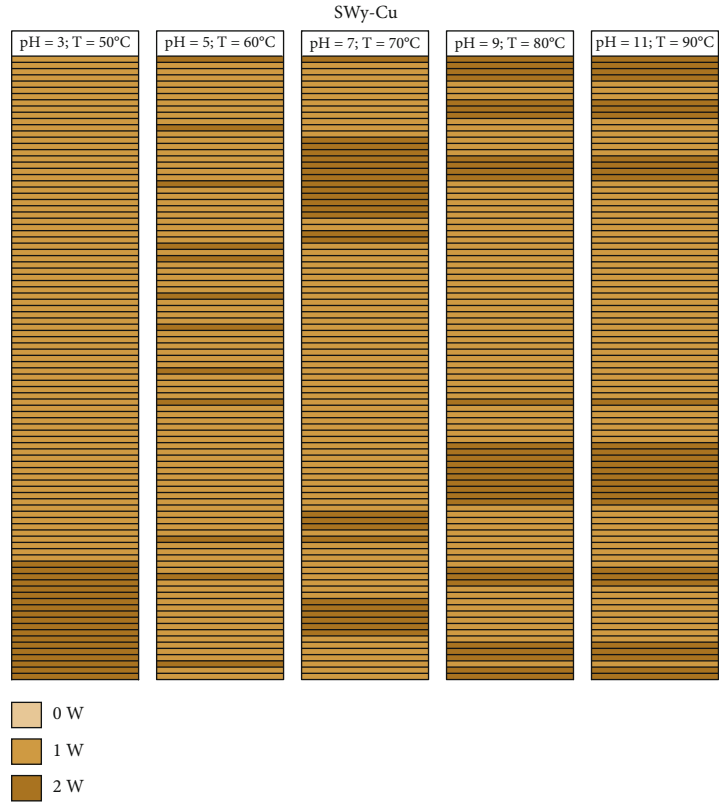

(b)

Figure 11: Continued.

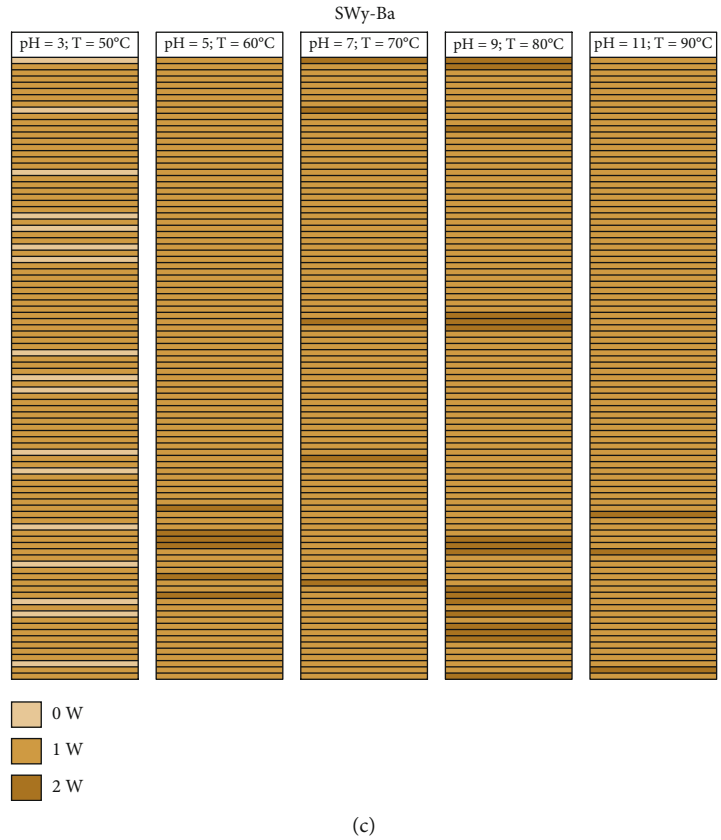

(c)

Figure 11: Mapping representation of the hydration state in the case of SWy-Co (a), SWy-Cu (b), and SWy-Ba (c) samples via XRD modeling approach.

applied. So, a regression approach based on the Lorentz equation was adopted to fit this evolution. This variation is described by function below:

$$y = y_0 + \left\{ \left(\frac{2A}{n} \right) \times \left(\frac{w}{4(x - x_c)^2 w^2} \right) \right\}, \quad (5)$$

where y_0 is the baseline offset, x_c is the center of the peak, w equals the width of the peak at half height, and A is the area under the peak. The parameters of the used Lorentz function are presented in Figure 9.

This decrease trends on the water molecule amount (nH_2O) versus constraint strength are predictable when increasing temperature which automatically affects the IS closing and subsequently, it affects the cation exchange capacity of the mineral.

3.5.2. Individual Evolution of the 0 W, 1 W, and 2 W Abundances versus Constraint Strength. The "water footprint" schematized on Figure S2 shows the coexistence within the particle of several phases with different weights. The variation of the cation exchange process makes it possible to better understand the structural response of the starting material (such as fluctuations in basal distance d_{001} , FWHM, crystalline size, rationality ξ, average number of layers M, and mode of stacking layers). Understanding the CEC functioning mode is closely related to the discretization of hydration states [48].

For SWy-Co samples, a decrease in the 1 W monohydrate state, accompanied by an increase in fluctuation for the 2 W hydration state, represents the main hydration behavior. This can be interpreted by an easy intercalation of the compensating cations (Co^{2+}) in IS more and more, replacing the sodium cations (Na^+) that will leave the structure partially according to the applied stress variation. This hypothesis is confirmed by the global incomplete exchange process despite the exchange equilibrium time provided and remains to be noted that abundances in the aqueous phase are normalized to 100%. For SWy-Cu samples, the same behavior of the previous sample (SWy-Co) is observed. A slight fluctuation for the 1 W hydration state followed by a slow increase of 2 W is noted. For the latest SWy-Ba samples, the water behavior is almost different. There is a slow decrease in the 1 W state. This fluctuation is accompanied by a slight increase of 2 W phases. This is not valid for the complex pH = 11 and $T = 90°C$ (extreme case) which has a minority anhydrate state of 0 W (15%) and a majority hydration state of 1 W (85%). The abundance of individual layer type deduced from the optimized theoretical MLS used to reproduce experimental XRD profiles was shown in Figure S3. Indeed, the 2 W hydration state is the most dominant phase in the entire SWy-Co series. Unlike the two complexes SWy-Cu and SWy-Ba, the 1 W hydration state is the most dominant phases.

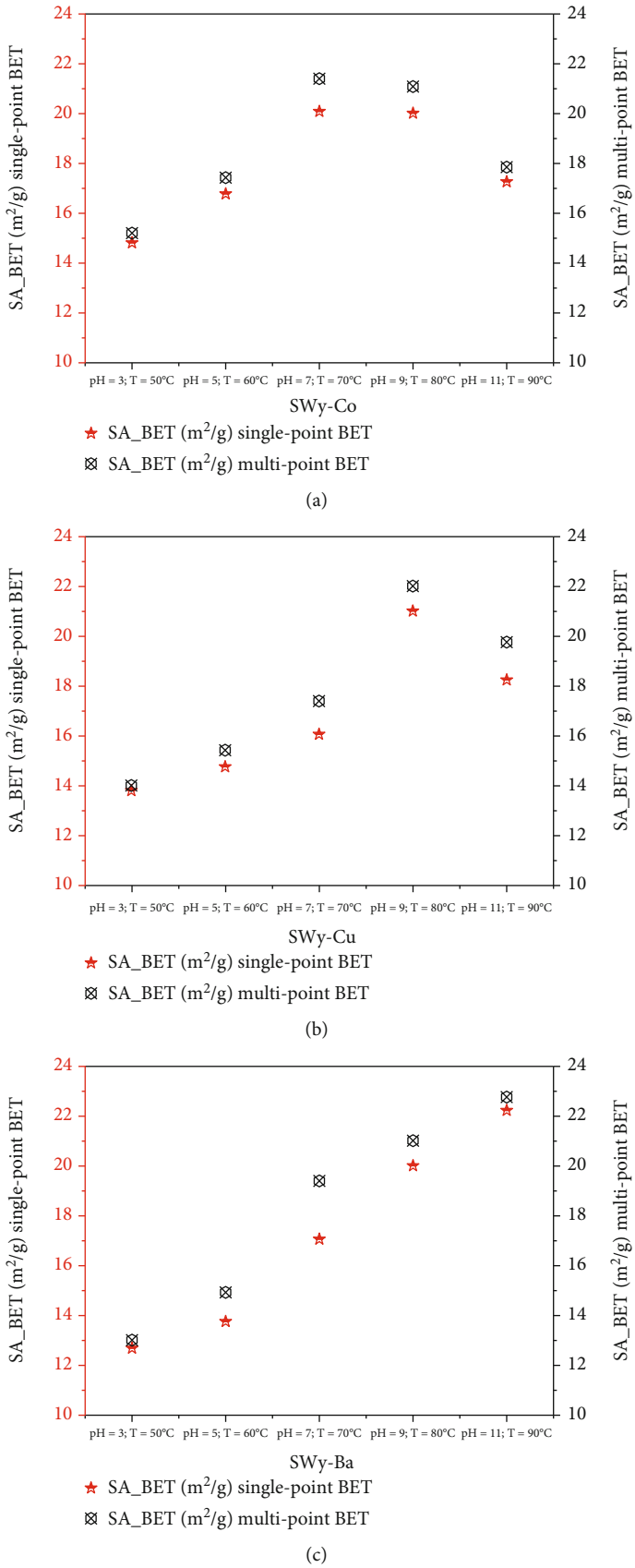

Figure 12: SA_{BET} single and multipoint BET evolution versus constraint strength for (a) SWy-Co, (b) SWy-Cu, and (c) SWy-Ba samples.

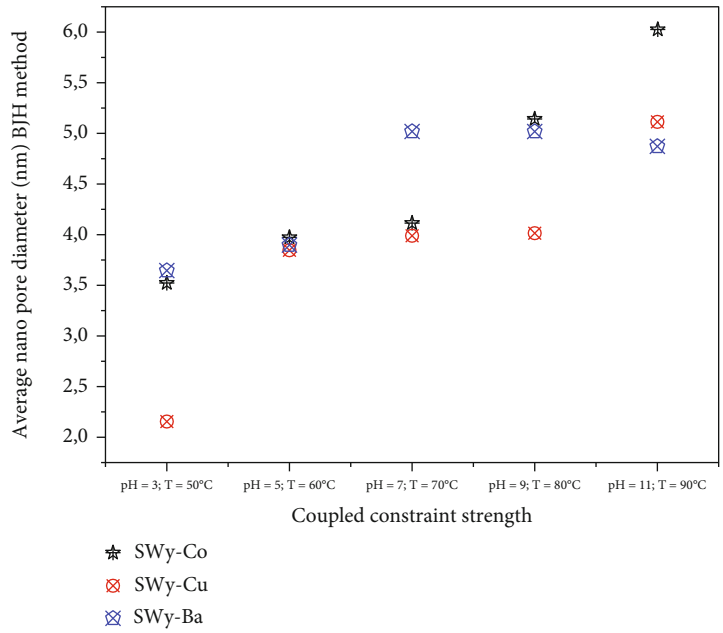

Figure 13: BJH method average pore diameter evolution versus constraint strength.

3.6. Evolution of the Average Number of Layers versus Constraint Strength. The average number of layers (M) is a very important parameter in the crystal structure clay response when studied by XRD analysis. It has a direct influence on the 001 reflections of the theoretical and experimental models. For the low M value, the reflections 001 will be very wide with elevated value of FMWH and vice versa. The evolution of M parameter for all SWy-Co, SWy-Cu, and SWy-Ba samples is shown in Figure 10.

The SWy-Ba sample is the exception and exhibits growth of M when increasing intensity constraint. The M evolution as a function of the applied stress applied is fitted for each sample and shown in Figure 10.

The evolution of M for all complexes following a Boltzmann function is shown below:

$$y = A_2 + \left\{\frac{(A_1 - A_2)}{1 + e^{(x - x_0/\mathrm{dx})}}\right\}, \quad (6)$$

where A_1 is the initial value, A_2 is the final value, x_0 is the center, and dx is a time constant.

All functions parameters are summarized in Figure 10.

3.7. Evolution of the Layer Stacking Modes. A mapping representation of the hydration state in the case of SWy-Co, SWy-Cu, and SWy-Ba samples via XRD modeling profile approach is summarized in Figure 11. The light brown, caramel, and dark brown colors represent the 0 W, 1 W, and 2 W layer type, respectively. Each line thus represents a layer with its intrinsic hydration state. The configuration considered here is an optimal configuration (best agreement obtained) extracted from the best agreements obtained between theoretical and experimental XRD profile. For SWy-Co complexes, the correlation between partial and total segregation stacking is observed. Thus, for SWy-Cu samples, we notice that the total segregation aspect is present regardless of the applied constraint applied. On the other hand, the SWy-Ba series shows the existence of two modes of stacking, segregation accompanied by partial order, with blatant dominance for segregated stacking.

3.8. BET and BJH Pore Size Distribution Analysis. The exploitation of the results obtained from the structural analysis by XRD modeling approach demonstrates a variability, in term of population, within the same crystallite. This directly influences the internal and external layers surfaces, which subsequently affects the adsorption properties and the sample porosity. Our objective is to evaluate the effect of the applied coupling disturbance (pH and T°C) on these properties. Indeed, we are looking for a link between structural damage, the intrinsic properties of the sample, and the saturation of the CEC. For that, a study based on BET adsorption measurement and BJH pore size distribution analysis is directed. Both the single-point and multipoint BET methods based on the surface area (SA) purpose from nitrogen isotherms were approved to evaluate external layer surface perturbation [41, 123–131] (Figure 12). Average pore diameter is determined using the BJH method (Figure 13). Whatever the nature of the exchangeable cation, an increase in the SA values is shown as a function of the constraint intensity up to a pH = 9 and a T = 80°C. After this limit value, a behavior divergence is shown. In fact, for the two samples saturated, respectively, by Co and Cu cations, a decrease in the SA values is observed against the continuous growth in the case of the Ba cation.

The average pore diameter evolution versus constraint strength (Figure 13) can provide a preliminary explanation for the observed SA fluctuations.

For all samples, the limit of mesoporosity domain is respected (where pores whose maximum diameter is

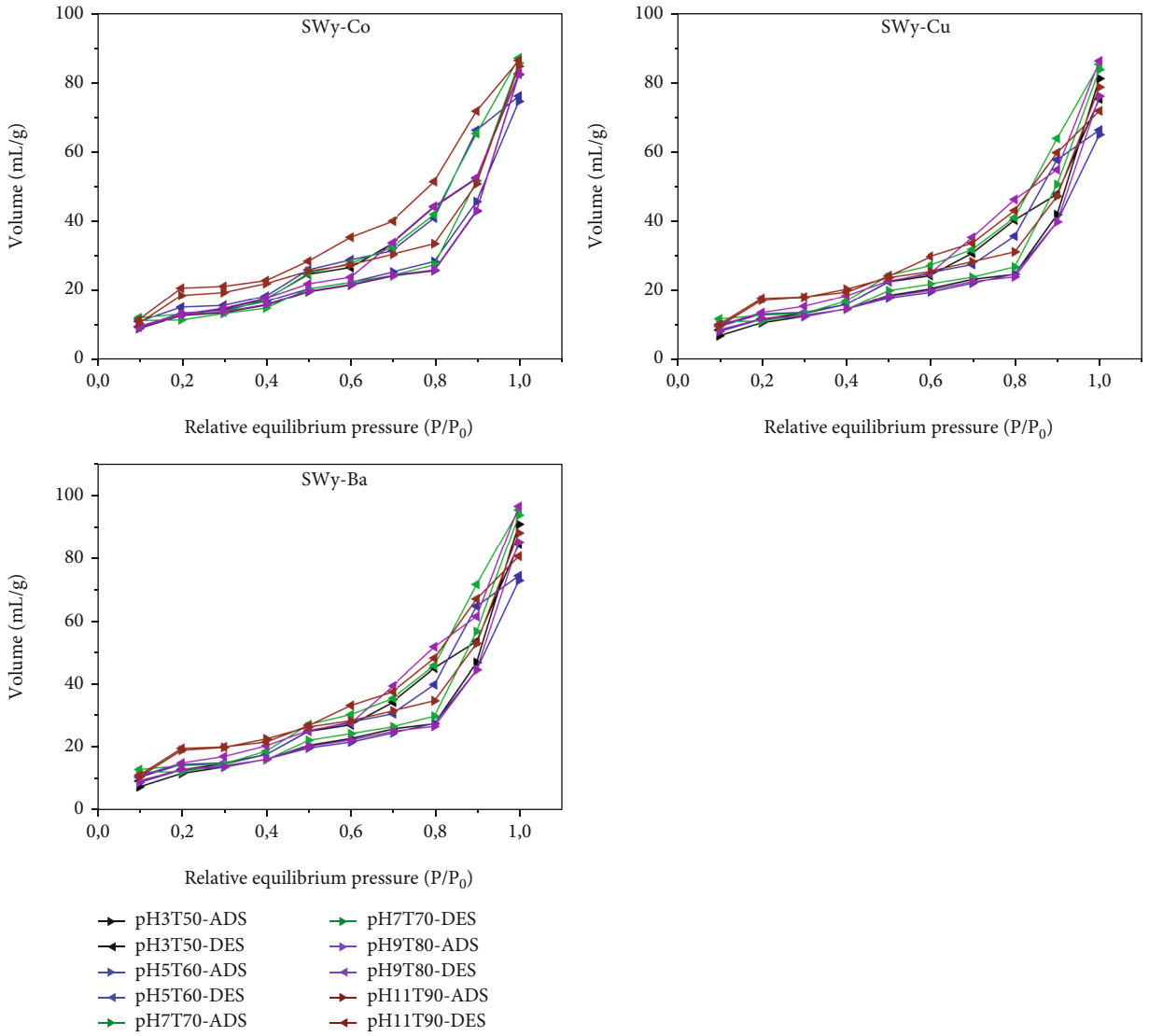

Figure 14: Nitrogen adsorption (ads)-desorption (des)-isotherms in the case of SWy-Co, SWy-Cu, and SWy-Ba.

between 2 and 50 nm). Indeed, the SWy-Ba sample practically keeps the same average pore diameters values up to pH = 11 and $T = 90°C$. However, the other two samples are marked by a considerable increase in the average pore diameter, which probably indicates a transformation that affected the internal configuration of the clay particle. This agrees with the results obtained from XRD analysis focusing the evolution of the average number of layers versus constraint strength.

Obtained nitrogen adsorption (ADS)-desorption (DES) isotherms curves shape (Figure 14) shows a very closer type II isotherm classification [127–131]. This allocation confirms the supremacy of the mesoporous texture despite the fluctuations observed and the nature of the exchangeable cation. The relative large pore size obtained in the case of stressed SWy-Ba sample is explained by the coupling of three essential parameters, respectively, the acidic or basic nature of the soil solution, the intrinsic hydration property, and the nature of the exchangeable cation. The Ba^{2+} ions exchange promotes the exfoliation process and thereafter increases the porosity degree.

To overcome the limits of SA analysis (i.e., nitrogen can only cover external surfaces and does not interact with internal surfaces), since it cannot access the information in the volume of the sample and subsequently, it does not provide information on the IS configurations/changes, a pore size distribution (PSD) analysis imposes itself. The application of PSD analysis requires technical approaches such as (i) the volumes of micropores, mesopores, and macropores including nanopores in one gram solid labeled, respectively, V_{Mi}, V_{Me}, and V_{Ma} (all in mL/g) and (ii) the effects related to macroporosity are neglected assuming that they do not affect the properties of adsorption and the specific micromesopore volumes ($V = V_{Mi} + V_{Me}$) that is determined using the desorption data (at the relative equilibrium pressure P/P_0). Fundamental approximations used for the PSD analysis target the shape and characteristics of the pores. Indeed, cylindrical shape (with radius (r) approximately half of its

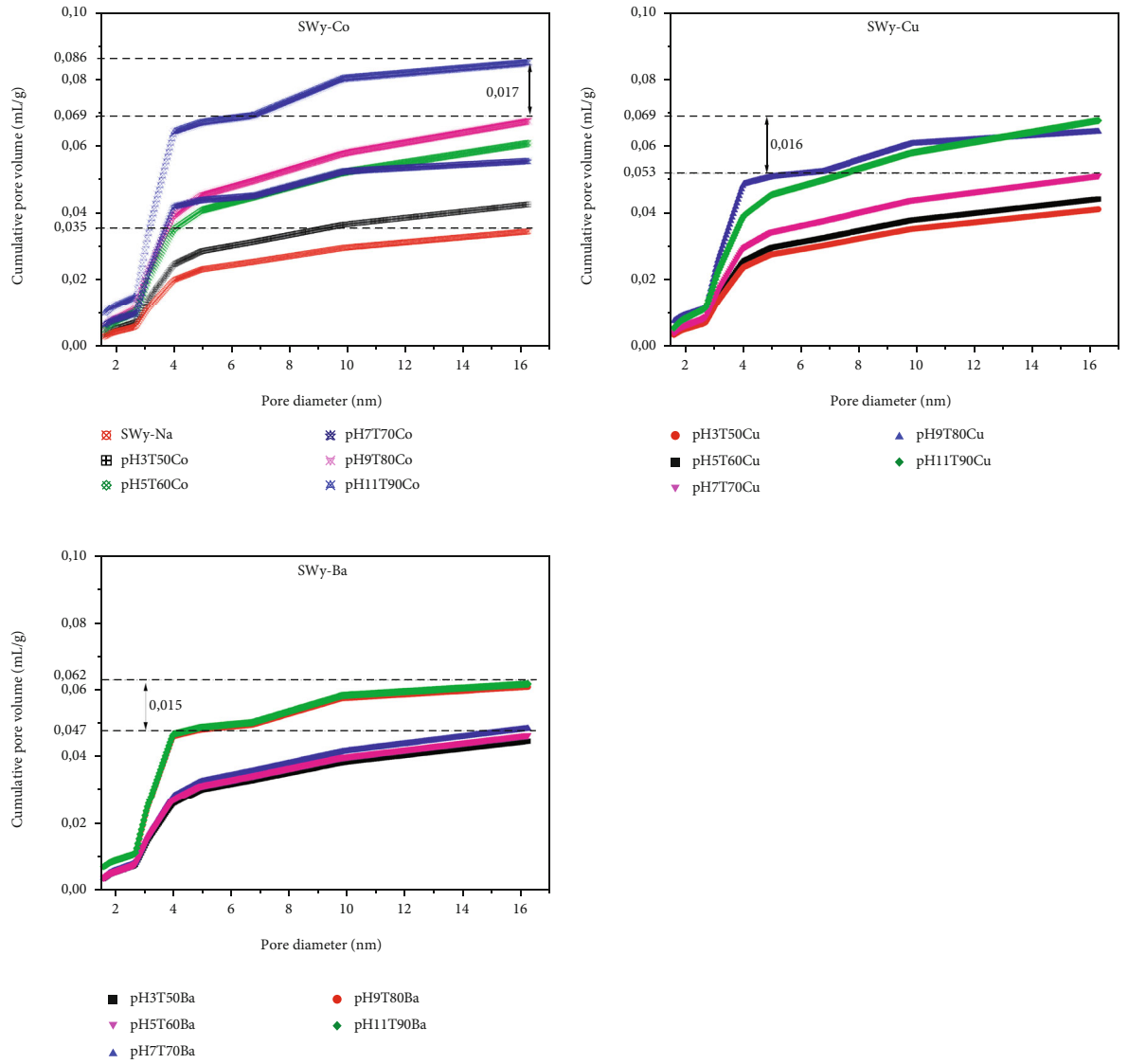

Figure 15: The pore size distribution (PSD) curve for the different studied samples (V-r) in the case of SWy-Co, SWy-Cu, and SWy-Ba.

width) is adopted. Also, cylindrical mesopores are characterized by r radii which correspond to V values (calculated from the corrected Kelvin equation using P/P_0 values).

The PSD plots provide information on the variation of the cumulative pore volume versus pore radius (V-r) (Figure 15). Although they have the same trend, the V-r curves relating to each sample present specificities showing the effect of the applied stress on the evolution of the porosity. In the case of SWy-Co sample and from a diameter of 4 nm, an evolution divergence appears with a "gap" in favor of high pH and T°C value which reaches 0.086 mL/g (Figure 15). The V-r variation divergence proves, initially, the achievement of the cation exchange process which is confirmed by an individual comportment of the V-r curves despite having the same appearance. In addition, a direct effect of the increase of the applied stresses appears as an increase in the V-r "gap." For SWy-Ba, the maximum cumulative pore volume is 0.062 mL/g attained at pH = 9 and T = 80°C. The major remark concerns the last two values of pH and T. Indeed, although they present a very similar appearance to the other V-r characteristic curves, there is a jump ("gap") of 0.015 mL/g attributed to the acid-base transformation. In the case of SWy-Cu, the V-r curves have respected the same shape as for the other samples, but the maximum value did not exceed 0.069 mL/g. The common behavior for the three samples lies in the existence of a cumulative pore volume "gap" observed during the acid-base transformation. The value of this gap is practically very similar and close for all samples, and it averages around 0.016 mL/g. This variation is consistent with the XRD modeling profile which predicts layer exfoliation and presence of highly hydrated rate.

The derivative pore size distribution curve (Figure 16) confirms the prevailing mesoporosity with a pore diameter concentration varying between 2.20 and 9.89 nm. A concentration of large pore populations related to the saturated

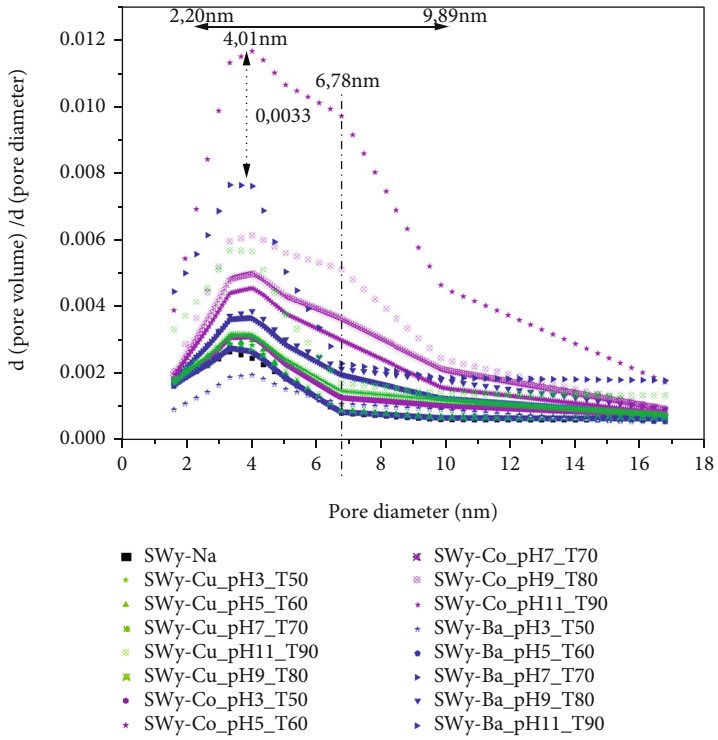

Figure 16: The derivative pore size distribution curve.

Co^{2+} sample (at pH = 11 and $T = 90°C$) is observed. This agrees with the obtained SA results and XRD analysis. The V-r curve radius derivative for all samples is given in Figure 16. For the rest of the studied samples, an almost similar variation is observed except for SWy-Ba (pH = 11/T = 90) which presents an extremum around 4.01 nm with a small extent.

4. Conclusion

This work studied the Wyoming montmorillonite response to a first-order coupling constraint obtained at the laboratory scale by combining soil solution pH variation with temperature gradient. The eventual mineral response to such disturbance was approached from a structural, hydrological (IS perturbation), cation exchange (CEC), and porosity point of view.

The quantitative investigation of the 001 reflections obtained from the XRD patterns via the modeling approach makes it possible to develop a deep theoretical calculation which allows us to build a global idea about the mechanisms accompanying these changes. Indeed, IS configuration and evolution are decrypted according to the applied constraint. Several parameters like nature, abundance, relative probability, size, position, arrangement of atoms/ions in the IS, the quantity of nH_2O, the average number of sheets, and the stacking modes in crystallites are precisely identified.

These goals are achieved by combining results from XRD profile modeling approach, TG/DTA analysis, and the adsorption measurement outcomes.

The starting SWy-Na complexes studied at room condition exhibit a heterogeneous hydration state characterized by a mixture between 0 W and 1 W phases contrary to the qualitative analysis which shows a homogeneous character. A correlation between XRD profile modeling approach consolidated by TG/DTA analysis and the adsorption measurement outcomes shows the following:

The case of the Co^{2+} cation is as follows:

(i) Heterogeneous hydration behavior induced by the coexistence of two type of layer populations (i.e., 1 W and 2 W phases within the crystallite), whatever the stress force

(ii) The theoretical decomposition of the experimental XRD profiles allowed us to identify all the different populations of existing layers and their stacking mode

(iii) A dominance of the segregated layer stacking mode

(iv) The CEC increases simultaneously with the applied stress intensity increases

(v) A linear regression approach describes the water molecule amount decrease, determined from TG/DTA analysis, as the temperature increases

(vi) The total structure change may appear ($2:1 \longrightarrow 1:1$) by exceeding the limit of the applied stress (pH 11 and $T > 150°C$)

(vii) The BJH method shows an increase on the porosity rate traduced by an evolution divergence appearing with a "gap" in favor of high pH and T°C value. The

pore diameter concentration is varying between 2.20 and 9.89 nm

The case of the Cu^{2+} cation is as follows:

(i) An interstratification explains the coexistence of two hydration states (1 W and 2 W) regardless of the stress strength

(ii) The coexistence within the crystallite of different types of layer populations stacked according to a specific set of junction probabilities

(iii) "Total segregation" stacking mode dominated the entire series

(iv) CEC growth by increasing the applied stress

(v) A nonlinear water molecules amount decrease unlike SWy-Co sample as a function of the increase in external applied stresses (from TG/DTA analysis) is fitted with a regression approach based on the Lorentz model

(vi) Adsorption outcomes demonstrate that the sample seems undamaged by the applied stress intensity fluctuations

The case of the Ba^{2+} cation is as follows:

(i) A heterogeneous hydration state proven by the presence of several layers 0 W, 1 W, and 2 W, regardless of the applied stress

(ii) The coexistence of several types of compensating cation (Ba^{2+} and Na^{+}) indicating the formation of a real physical mixture between populations of different layer types

(iii) Partial CEC saturation and domination of segregated layer stacking aspect

(iv) Results from TG/DTA analysis show a nonlinear evolution governed by a Lorentz function which lies between the observed evolution in the case of Co^{2+} and Cu^{2+} cations

(v) The intrinsic sample porosity is affected by the acid-base transformation with a 0.015 mL/g "gap." The maximum cumulative pore volume is 0.062 mL/g attained at pH = 9 and $T = 80°C$

In addition, the XRD modeling approach allowed us to assign a structural response of the water footprint of the samples and to map the interstratification of the different layer type populations.

The presence of each cation induces specific structural characteristics and a variable exchanged sample response to external excitation. The observed structural transition, for the Co^{2+} cation from a pH = 8 and $T = 80°$, accompanied by a concentration of large pore populations (at pH = 11 and $T = 90°C$) indicates the strong exfoliation phenomena affecting even the elementary tetrahedral or octahedral sheets and subsequently reducing the metal removal efficiency.

The evolution of the average number of layers (M) confirms the consolidation of the crystallite thickness in the case of Ba^{2+} cation despite the acid-base transition and the strong thermal gradient. This is in favor of an irreversible cation exchange process supporting the Barium removal efficiency.

Data Availability

No data were used to support this study.

Disclosure

The results presented are a part of the Ph.D. thesis of Chadha MEJRI (CM) realized at LR19ES20: Resources, Materials, and Ecosystems (RME), Faculty of Sciences of Bizerte, University of Carthage, 7021 Zarzouna, Tunisia, and supervised by Dr. Walid Oueslati (WO).

Conflicts of Interest

The authors declare no conflict of interest.

Authors' Contributions

Ph.D. Chadha MEJRI (CM) realized the experimental part, XRD profile modeling approach, and the draft paper writing. Dr. Walid Oueslati (WO) supervised the study, contributed to the experimental result acquisition and XRD profile modeling approach, realized the adsorption measurement, directed the (BJH) pore size distribution analyses, and contributed on the writing of the paper draft and the proof reading/revision of the manuscript.

Acknowledgments

CM acknowledges WO for the original idea of the work, the fruitful discussions about the XRD modeling approach, and the montmorillonite hydration behavior.

Supplementary Materials

Figure S1: results of thermogravimetry/differential thermal analysis (TG/DTA) for the samples SWy-Co, SWy-Cu, and SWy-Ba. Figure S2: scheme of the "Water Footprint" of SWy-Co, SWy-Cu, and SWy-Ba samples via X-ray diffraction modeling. The light brown, caramel, and dark brown colors represent the hydration states of the layers of type 0 W, 1 W, and 2 W, respectively, related to each phase. Figure S3: evolutions in the percentage of hydration layer types for samples SWy-Co, SWy-Cu, and SWy-Ba. *(Supplementary Materials)*

References

[1] G. Brown, "Crystal structures of clay minerals and their X-ray identification," *The Mineralogical Society of Great Britain and Ireland*, vol. 5, pp. 1–494, 1982.

[2] A. C. D. Newman, "Chemistry of clays and clay minerals," *Mineral Society Monograph, London*, vol. 6, pp. 1–480, 1987.

[3] N. Güven, "Hydrous phyllosilicates (exclusive of micas)," in *Reviews in Mineralogy*, S. W. Bailey, Ed., vol. 19, pp. 1–497, Walter de Gruyter GmbH & Co KG, 1988.

[4] W. F. Moll, "Baseline studies of the clay minerals society source clays: geological origin," *Clays and Clay Minerals*, vol. 49, no. 5, pp. 374–380, 2001.

[5] T. Sato, T. Watanabe, and R. Otsuka, "Effects of layer charge, charge location, and energy change on expansion properties of dioctahedral smectites," *Clays and Clay Minerals*, vol. 40, no. 1, pp. 103–113, 1992.

[6] I. Bérend, J. M. Cases, M. François et al., "Mechanism of adsorption and desorption of water vapor by homoionic montmorillonites: 2. The Li^+, Na^+, K^+, Rb^+, and Cs^+-exchanged forms," *Clays and Clay Minerals*, vol. 43, no. 3, pp. 324–336, 1995.

[7] J. M. Cases, I. Bérend, M. François, J. P. Uriot, L. J. Michot, and F. Thomas, "Mechanism of adsorption and desorption of water vapor by homoionic montmorillonite: 3. The Mg^{2+}, Ca2+, Sr^{2+} and Ba^{2+} exchanged forms," *Clays and Clay Minerals*, vol. 45, no. 1, pp. 8–22, 1997.

[8] I. Nistor and N. Miron, "Depollution of uranyl polluted waters using pillared clays," *Journal of Thermal Analysis and Calorimetry*, vol. 89, no. 3, pp. 977–981, 2007.

[9] I. Chaari, M. Medhioub, and F. Jamoussi, "Use of clay to remove heavy metals from Jebel Chakir landfill leachate," *Journal of Applied Sciences in Environmental Sanitation*, vol. 6, no. 2, pp. 143–148, 2011.

[10] L. N. F. de Queiroga, D. B. França, F. Rodrigues, I. M. G. Santos, M. G. Fonseca, and M. Jaber, "Functionalized bentonites for dye adsorption: Depollution and production of new pigments," *Journal of Environmental Chemical Engineering*, vol. 7, no. 5, article 103333, 2019.

[11] J. G. Mahy, M. H. Tsaffo Mbognou, C. Léonard, N. Fagel, E. D. Woumfo, and S. D. Lambert, "Natural clay modified with ZnO/TiO_2 to enhance pollutant removal from water," *Catalysts*, vol. 12, no. 2, pp. 148–148, 2022.

[12] M. L. Whittaker, L. N. Lammers, S. Carrero, B. Gilbert, and J. F. Banfield, "Ion exchange selectivity in clay is controlled by nanoscale chemical–mechanical coupling," *Proceedings of the National Academy of Sciences*, vol. 116, no. 44, pp. 22052–22057, 2019.

[13] G. Moldoveanu and V. Papangelakis, "Chelation-assisted ion-exchange leaching of rare earths from clay minerals," *Metals*, vol. 11, no. 8, pp. 1265–1279, 2021.

[14] S. T. Hussain and S. A. K. Ali, "Removal of heavy metal by ion exchange using bentonite clay," *Journal of Ecological Engineering*, vol. 22, no. 1, pp. 104–111, 2021.

[15] N. Subramanian and L. N. Lammers, "Thermodynamics of ion exchange coupled with swelling reactions in hydrated clay minerals," *Journal of Colloid and Interface Science*, vol. 608, pp. 692–701, 2022.

[16] H. S. D. C. Neves, T. L. da Silva, M. G. C. da Silva, R. Guirardello, and M. G. A. Vieira, "Ion exchange and adsorption of cadmium from aqueous media in sodium-modified expanded vermiculite," *Environmental Science and Pollution Research*, vol. 2022, pp. 1–17, 2022.

[17] J. L. Bobin, E. Huffer, and H. Nifenecker, "Le stockage des déchets nucléaires en site profond," in *L'énergie de demain: Techniques, environnement, économie*, pp. 429–448, Les Ulis: EDP Sciences, 2021.

[18] A. Usuki, N. Hasegawa, M. Kato, and S. Kobayashi, "Polymer-clay nanocomposites," *Inorganic Polymeric Nanocomposites and Membranes*, vol. 179, pp. 135–195, 2005.

[19] G. Choudalakis and A. D. Gotsis, "Permeability of polymer/clay nanocomposites: a review," *European Polymer Journal*, vol. 45, no. 4, pp. 967–984, 2009.

[20] M. Raji, M. E. M. Mekhzoum, D. Rodrigue, and R. Bouhfid, "Effect of silane functionalization on properties of polypropylene/clay nanocomposites," *Composites Part B: Engineering*, vol. 146, pp. 106–115, 2018.

[21] S. Murugesan and T. Scheibel, "Copolymer/clay nanocomposites for biomedical applications," *Advanced Functional Materials*, vol. 30, no. 17, pp. 1908101–1908129, 2020.

[22] B. Qu and Y. Luo, "A review on the preparation and characterization of chitosan-clay nanocomposite films and coatings for food packaging applications," *Carbohydrate Polymer Technologies and Applications*, vol. 2, pp. 100102–100112, 2021.

[23] Z. Ghorbani, N. Zamindar, S. Baghersad, S. Paidari, S. M. Jafari, and L. Khazdooz, "Evaluation of quality attributes of grated carrot packaged within polypropylene-clay nanocomposites," *Journal of Food Measurement and Characterization*, vol. 15, no. 4, pp. 3770–3781, 2021.

[24] M. R. Abass, E. H. El-Masry, and A. B. Ibrahim, "Preparation, characterization, and applications of polyacrylonitrile/ball clay nanocomposite synthesized by gamma radiation," *Environmental Geochemistry and Health*, vol. 43, no. 8, pp. 3169–3188, 2021.

[25] Y. Zhu, J. O. Iroh, R. Rajagopolan, A. Aykanat, and R. Vaia, "Optimizing the synthesis and thermal properties of conducting polymer–montmorillonite clay nanocomposites," *Energies*, vol. 15, no. 4, pp. 1218–1291, 2022.

[26] M. Razavi, N. Sadeghi, S. H. Jafari, H. A. Khonakdar, U. Wagenknecht, and A. Leuteritz, "Thermo-rheological probe of microstructural evolution and degradation pathway in the flame-retarded PP/EVA/NOR/clay nanocomposites," *Rheologica Acta*, vol. 61, no. 1, pp. 25–47, 2022.

[27] A. Teepakakorn, T. Hayakawa, and M. Ogawa, "Remarkable stability of dye in polymer-clay nanocomposite film," *Applied Clay Science*, vol. 218, article 106405, 2022.

[28] M. I. Carretero and M. Pozo, "Clay and non-clay minerals in the pharmaceutical and cosmetic industries part II. Active ingredients," *Applied Clay Science*, vol. 47, no. 3-4, pp. 171–181, 2010.

[29] A. Papadopoulos, K. Giouri, E. Tzamos, A. Filippidis, and S. Stoulos, "Natural radioactivity and trace element composition of natural clays used as cosmetic products in the Greek market," *Clay Minerals*, vol. 49, no. 1, pp. 53–62, 2014.

[30] A. Panchal, G. Fakhrullina, R. Fakhrullin, and Y. Lvov, "Self-assembly of clay nanotubes on hair surface for medical and cosmetic formulations," *Nanoscale*, vol. 10, no. 38, pp. 18205–18216, 2018.

[31] J. Gubitosa, V. Rizzi, P. Fini, and P. Cosma, "Hair care cosmetics: from traditional shampoo to solid clay and herbal shampoo, a review," *Cosmetics*, vol. 6, no. 1, pp. 13–29, 2019.

[32] C. D. S. F. Gomes and J. B. P. Silva, "Minerals and clay minerals in medical geology," *Applied Clay Science*, vol. 36, no. 1-3, pp. 4–21, 2007.

[33] M. I. Carretero and M. Pozo, "Clay and non-clay minerals in the pharmaceutical industry: part I. excipients and medical applications," *Applied Clay Science*, vol. 46, no. 1, pp. 73–80, 2009.

[34] M. Massaro, G. Lazzara, S. Milioto, R. Noto, and S. Riela, "Covalently modified halloysite clay nanotubes: synthesis, properties, biological and medical applications," *Journal of Materials Chemistry B*, vol. 5, no. 16, pp. 2867–2882, 2017.

[35] S. M. Mousavi, S. A. Hashemi, S. Salahi, M. Hosseini, A. M. Amani, and A. Babapoor, "Development of clay nanoparticles toward bio and medical applications," in *In Current Topics in the Utilization of Clay in Industrial and Medical Applications*, pp. 167–191, Intech Open, London, UK, 2018.

[36] L. B. Williams and S. E. Haydel, "Evaluation of the medicinal use of clay minerals as antibacterial agents," *International Geology Review*, vol. 52, no. 7-8, pp. 745–770, 2010.

[37] L. B. Williams, D. W. Metge, D. D. Eberl et al., "What makes a natural clay antibacterial?," *Environmental Science & Technology*, vol. 45, no. 8, pp. 3768–3773, 2011.

[38] K. D. Morrison, J. C. Underwood, D. W. Metge, D. D. Eberl, and L. B. Williams, "Mineralogical variables that control the antibacterial effectiveness of a natural clay deposit," *Environmental Geochemistry and Health*, vol. 36, no. 4, pp. 613–631, 2014.

[39] L. Zarate-Reyes, C. Lopez-Pacheco, A. Nieto-Camacho et al., "Antibacterial clay against gram-negative antibiotic resistant bacteria," *Journal of Hazardous Materials*, vol. 342, pp. 625–632, 2018.

[40] B. Dazas, E. Ferrage, A. Delville, and B. Lanson, "Interlayer structure model of tri-hydrated low-charge smectite by X-ray diffraction and Monte Carlo modeling in the grand canonical ensemble," *American Mineralogist*, vol. 99, no. 8-9, pp. 1724–1735, 2014.

[41] C. Mejri, W. Oueslati, and A. B. H. Amara, "How the solid/liquid ratio affects the cation exchange process and porosity in the case of dioctahedral smectite: structural analysis?," *Adsorption Science and Technology*, vol. 2021, pp. 1–24, 2021.

[42] V. A. Drits, C. Tchoubar, V. A. Drits, and C. Tchoubar, "Experimental Techniques Adapted to the Study of Microdivided Lamellar Systems," in *In X-Ray Diffraction by Disordered Lamellar Structures*, pp. 165–198, Springer, Berlin, Heidelberg, 1990.

[43] A. R. Mermut and A. F. Cano, "Baseline studies of the clay minerals society source clays: chemical analyses of major elements," *Clays and Clay Minerals*, vol. 49, no. 5, pp. 381–386, 2001.

[44] M. Segad, B. Jonsson, T. Åkesson, and B. Cabane, "Ca/Na montmorillonite: structure, forces and swelling properties," *Langmuir*, vol. 26, no. 8, pp. 5782–5790, 2010.

[45] K. Yotsuji, Y. Tachi, H. Sakuma, and K. Kawamura, "Effect of interlayer cations on montmorillonite swelling: comparison between molecular dynamic simulations and experiments," *Applied Clay Science*, vol. 204, article 106034, 2021.

[46] H. Yan and Z. Zhang, "Effect and mechanism of cation species on the gel properties of montmorillonite," *Colloids and Surfaces A: Physicochemical and Engineering Aspects*, vol. 611, article 125824, 2021.

[47] W. Oueslati, H. B. Rhaiem, and A. B. H. Amara, "XRD investigations of hydrated homoionic montmorillonite saturated by several heavy metal cations," *Desalination*, vol. 271, no. 1-3, pp. 139–149, 2011.

[48] W. Oueslati and M. Meftah, "Discretization of the water uptake process of Na-montmorillonite undergoing atmospheric stress: XRD modeling approach," *Advances in Materials Science and Engineering*, vol. 2018, 17 pages, 2018.

[49] B. Dazas, B. Lanson, J. Breu, J. L. Robert, M. Pelletier, and E. Ferrage, "Smectite fluorination and its impact on interlayer water content and structure: a way to fine tune the hydrophilicity of clay surfaces?," *Microporous and Mesoporous Materials*, vol. 181, pp. 233–247, 2013.

[50] S. Gu, X. Kang, L. Wang, E. Lichtfouse, and C. Wang, "Clay mineral adsorbents for heavy metal removal from wastewater: a review," *Environmental Chemistry Letters*, vol. 17, no. 2, pp. 629–654, 2019.

[51] B. O. Otunola and O. O. Ololade, "A review on the application of clay minerals as heavy metal adsorbents for remediation purposes," *Environmental Technology and Innovation*, vol. 18, article 100692, 2020.

[52] S. Yingying, Z. Baoqiang, and W. Yang, "Application of clay minerals in remediation of heavy metal pollution in soil," *EDP Sciences*, vol. 204, p. 01011, 2020.

[53] A. R. A. Usman, Y. Kuzyakov, and K. Stahr, "Effect of clay minerals on extractability of heavy metals and sewage sludge mineralization in soil," *Chemistry and Ecology*, vol. 20, no. 2, pp. 123–135, 2004.

[54] Y. Zhang, Y. Li, J. Li, L. Hu, and X. Zheng, "Enhanced removal of nitrate by a novel composite: nanoscale zero valent iron supported on pillared clay," *Chemical Engineering Journal*, vol. 171, no. 2, pp. 526–531, 2011.

[55] M. M. Wahba, B. F. Labib, K. H. M. Darwish, and M. A. Zaghloul, "Application of some clay minerals to eliminate the hazards of heavy metals in contaminated soils," in *15th International Conference on EnvironmentalScience And Technology*, Rhodes, Greece, 2017.

[56] G. D. Yuan, B. K. G. Theng, G. J. Churchman, and W. P. Gates, "Clays and clay minerals for pollution control," *In Developments in Clay Science, Elsevier*, vol. 5, pp. 587–644, 2013.

[57] P. Antoine, A. Marchiol, M. Brocandel, and Y. Gros, "Discovery of periglacial features (sand and composite-wedges) in the nuclear waste storage site of the Aube department (France)," *Comptes Rendus Geoscience*, vol. 337, no. 16, pp. 1462–1473, 2005.

[58] A. Dizier, *Caractérisation des effets de température dans la zone endommagée autour de tunnels de stockage de déchets nucléaires dans des roches argileuses[Doctoral dissertation]*, Université de Liège, Belgique, 2011.

[59] P. Landrein, G. Vigneron, J. Delay, P. Lebon, and M. Pagel, "Lithologie, hydrodynamisme et thermicité dans le système sédimentaire multicouche recoupé par les forages Andra de Montiers-sur-Saulx (Meuse)," *Bulletin de la Société géologique de France*, vol. 184, no. 6, pp. 519–543, 2013.

[60] P. M. Abadie, "La gestion des déchets radioactifs en France et dans le monde," *In Annales des Mines-Responsabilite et environnement, FFE*, vol. 97, no. 1, pp. 48–52, 2020.

[61] A. S. Anastácio, A. Aouad, P. Sellin, J. D. Fabris, F. Bergaya, and J. W. Stucki, "Characterization of a redox-modified clay mineral with respect to its suitability as a barrier in radioactive waste confinement," *Applied Clay Science*, vol. 39, no. 3-4, pp. 172–179, 2008.

[62] R. A. Schoonheydt, C. T. Johnston, M. F. Brigatti, and A. Mottana, "The surface properties of clay minerals," *EMU Notes Mineral*, vol. 11, no. 10, pp. 337–373, 2011.

[63] R. Pusch, S. Knutsson, L. Al-Taie, and M. Hatem, "Optimal ways of disposal of highly radioactive waste," *Natural Science*, vol. 4, no. 11, pp. 906–918, 2012.

[64] P. Sellin and O. X. Leupin, "The use of clay as an engineered barrier in radioactive-waste management–a review," *Clays and Clay Minerals*, vol. 61, no. 6, pp. 477–498, 2013.

[65] F. M. Huber, S. Heck, L. Truche et al., "Radionuclide desorption kinetics on synthetic Zn/Ni-labeled montmorillonite nanoparticles," *Geochimica et Cosmochimica Acta*, vol. 148, pp. 426–441, 2015.

[66] N. P. Laverov, S. V. Yudintsev, B. T. Kochkin, and V. I. Malkovsky, "The Russian strategy of using crystalline rock as a repository for nuclear waste," *Elements*, vol. 12, no. 4, pp. 253–256, 2016.

[67] C. A. Coles and R. N. Yong, "Aspects of kaolinite characterization and retention of Pb and cd," *Applied Clay Science*, vol. 22, no. 1-2, pp. 39–45, 2002.

[68] J. H. Potgieter, S. S. Potgieter-Vermaak, and P. D. Kalibantonga, "Heavy metals removal from solution by palygorskite clay," *Minerals Engineering*, vol. 19, no. 5, pp. 463–470, 2006.

[69] G. J. Churchman, W. P. Gates, B. K. G. Theng, and G. Yuan, "Chapter 11.1 clays and clay minerals for pollution control," *Developments in Clay Science*, vol. 1, pp. 625–675, 2006.

[70] D. Mohapatra, D. Mishra, G. R. Chaudhury, and R. P. Das, "Arsenic adsorption mechanism on clay minerals and its dependence on temperature," *Korean Journal of Chemical Engineering*, vol. 24, no. 3, pp. 426–430, 2007.

[71] R. Chalghaf, W. Oueslati, M. Ammar, H. B. Rhaiem, and A. B. H. Amara, "Effect of temperature and pH value on cation exchange performance of a natural clay for selective (Cu^{2+}, Co^{2+}) removal: equilibrium, sorption and kinetics," *Progress in Natural Science: Materials International*, vol. 23, no. 1, pp. 23–35, 2013.

[72] H. Es-Sahbany, M. Berradi, S. Nkhili et al., "Removal of heavy metals (nickel) contained in wastewater-models by the adsorption technique on natural clay," *Materials Today: Proceedings*, vol. 13, pp. 866–875, 2019.

[73] O. Vidal, A. Baldeyrou, D. Beaufort, B. Fritz, N. Geoffroy, and B. Lanson, "Experimental study of the stability and phase relations of clays at high temperature in a thermal gradient," *Clays and Clay Minerals*, vol. 60, no. 2, pp. 200–225, 2012.

[74] H. Yin and J. Zhu, "In situ remediation of metal contaminated lake sediment using naturally occurring, calcium-rich clay mineral-based low-cost amendment," *Chemical Engineering Journal*, vol. 285, pp. 112–120, 2016.

[75] D. E. Pufahl, D. G. Fredlund, and H. Rahardjo, "Lateral earth pressures in expansive clay soils," *Canadian Geotechnical Journal*, vol. 20, no. 2, pp. 228–241, 1983.

[76] I. Berend, "Les mécanismes d'hydratation de montmorillonites homoioniques pour des pressions relatives inferieures à 0.95, [Doctoral dissertation]," Institut National Polytechnique de Lorraine, 1991.

[77] W. Oueslati, M. S. Karmous, H. B. Rhaiem, B. Lanson, and A. B. H. Amara, "Effect of interlayer cation and relative humidity on the hydration properties of a dioctahedral smectite," *Zeitschrift für Kristallographie Supplements*, vol. 2007, supplement 26, pp. 417–422, 2007.

[78] W. Oueslati, H. B. Rhaiem, and A. B. H. Amara, "Effect of relative humidity constraint on the metal exchanged montmorillonite performance: an XRD profile modeling approach," *Applied Surface Science*, vol. 261, pp. 396–404, 2012.

[79] M. Ammar, W. Oueslati, N. Chorfi, and H. Ben Rhaiem, "Interlamellar space configuration under variable environmental conditions in the case of Ni-exchanged montmorillonite: quantitative XRD analysis," *Journal of Nanomaterials*, vol. 2014, 13 pages, 2014.

[80] W. Oueslati, N. Chorfi, and M. Abdelwahed, "Effect of mechanical constraint on the hydration properties of Na-montmorillonite: study under extreme relative humidity conditions," *Powder Diffraction*, vol. 32, no. S1, pp. S160–S167, 2017.

[81] W. Oueslati, "Effect of soil solution pH during the tetracycline intercalation on the structural properties of a dioctahedral smectite: microstructural analysis," *Journal of Nanomaterials*, vol. 2019, 17 pages, 2019.

[82] W. Oueslati, H. Ben Rhaiem, M. S. Karmous, S. Naaman, and A. B. H. Amara, "Study of the structural evolution and selectivity of Wyoming montmorillonite in relation with the concentration of Cu^{2+} and Ni^{2+}," *Zeitschrift für Kristallographie Supplement*, vol. 2006, supplement_23, pp. 425–429, 2006.

[83] M. S. Karmous, H. B. Rhaiem, J. L. Robert, B. Lanson, and A. B. H. Amara, "Charge location effect on the hydration properties of synthetic saponite and hectorite saturated by Na^{+}, Ca^{2+} cations: XRD investigation," *Applied Clay Science*, vol. 46, no. 1, pp. 43–50, 2009.

[84] M. Meftah, W. Oueslati, and A. B. H. Amara, "Synthesis of zeolites A and P from 1: 1 and HS from 2: 1 clays," *2nd International Conference on Materials Physics and Applications (JIPMA 2009/MATERIAUX 2009)*, vol. 13, 2010no. 1, Article ID 12019, 2010IOP Publishing, Gafsa, Tunisia, 2010.

[85] N. C. Marty, S. Grangeon, A. Lassin, B. Madé, P. Blanc, and B. Lanson, "A quantitative and mechanistic model for the coupling between chemistry and clay hydration," *Geochimica et Cosmochimica Acta*, vol. 283, pp. 124–135, 2020.

[86] V. Chantawong, N. W. Harvey, and V. N. Bashkin, "Comparison of heavy metal adsorptions by Thai kaolin and ballclay," *Water, Air, and Soil Pollution*, vol. 148, no. 1/4, pp. 111–125, 2003.

[87] A. Alshameri, H. He, C. Xin et al., "Understanding the role of natural clay minerals as effective adsorbents and alternative source of rare earth elements: adsorption operative parameters," *Hydrometallurgy*, vol. 185, pp. 149–161, 2019.

[88] D. M. K. Manohar, A. Krishnan, and T. S. Anirudhan, "Removal of mercury (II) from aqueous solutions and chlor-alkali industry wastewater using 2-mercaptobenzimidazole-clay," *Water Research*, vol. 36, no. 6, pp. 1609–1619, 2002.

[89] W. Zhang, Y. An, S. Li et al., "Enhanced heavy metal removal from an aqueous environment using an eco- friendly and sustainable adsorbent," *Scientific Reports*, vol. 10, no. 1, pp. 1–19, 2020.

[90] C. Zhang, L. Liu, Y. Dai, K. Zhu, Z. Liu, and H. Jia, "Molecular dynamics simulations of exchange behavior of radionuclides into montmorillonite: unraveling the dynamic processes and microscopic structures," *Applied Clay Science*, vol. 226, article 106579, 2022.

[91] L. Liu, C. Zhang, W. Jiang, X. Li, Y. Dai, and H. Jia, "Understanding the sorption behaviors of heavy metal ions in the interlayer and nanopore of montmorillonite: a molecular dynamics study," *Journal of Hazardous Materials*, vol. 416, article 125976, 2021.

[92] C. Zhang, X. Liu, R. M. Tinnacher, and C. Tournassat, "Mechanistic understanding of uranyl ion complexation on

montmorillonite edges: a combined first-principles molecular dynamics–surface complexation modeling approach," *Environmental Science and Technology*, vol. 52, no. 15, pp. 8501–8509, 2018.

[93] R. Hånde, V. Ramothe, S. Tesson et al., "Classical polarizable force field to study hydrated hectorite: optimization on DFT calculations and validation against XRD data," *Minerals*, vol. 8, no. 5, pp. 205–2021, 2018.

[94] E. Scholtzová and D. Tunega, "Density functional theory study of the stability of the tetrabutylphosphonium and tetrabutylammonium montmorillonites," *Clay Minerals*, vol. 54, no. 1, pp. 41–48, 2019.

[95] T. Ohkubo, T. Okamoto, K. Kawamura et al., "New insights into the Cs adsorption on montmorillonite clay from133Cs solid-state NMR and density functional theory calculations," *The Journal of Physical Chemistry A*, vol. 122, no. 48, pp. 9326–9337, 2018.

[96] C. Bataillon, C. Musy, and M. Roy, "Corrosion des surconteneurs de déchets, cas d'un surconteneur en acier faiblement allié," *Le Journal de Physique IV*, vol. 11, no. 1, pp. Pr1-267–Pr1-274, 2001.

[97] W. Oueslati, M. Ammar, and N. Chorfi, "Quantitative XRD analysis of the structural changes of Ba-exchanged montmorillonite: effect of an in situ hydrous perturbation," *Minerals*, vol. 5, no. 3, pp. 507–526, 2015.

[98] S. W. Bailey, "Structures of layer silicates," *Crystal Structures of Clay Minerals and their X-Ray Identification*, vol. 5, 1980.

[99] J. Ben Brahim, G. Besson, and C. Tchoubar, "Etude des profils des bandes de diffraction X d'une beidellite-Na hydratée à deux couches d'eau. Détermination du mode d'empilement des feuillets et des sites occupés par l'eau," *Journal of Applied Crystallography*, vol. 17, no. 3, pp. 179–188, 1984.

[100] B. A. Sakharov and B. Lanson, "X-ray identification of mixed-layer structures: modelling of diffraction effects," *In Developments in Clay Science, Elsevier*, vol. 5, pp. 51–135, 2013.

[101] E. Ferrage, B. Lanson, B. A. Sakharov, and V. A. Drits, "Investigation of smectite hydration properties by modeling experimental X-ray diffraction patterns: part I. Montmorillonite hydration properties," *American Mineralogist*, vol. 90, no. 8-9, pp. 1358–1374, 2005.

[102] B. Lanson, "Modelling of X-ray diffraction profiles," *EMU Notes in Mineralogy*, vol. 11, no. 4, pp. 151–202, 2011.

[103] B. A. Sakharov and V. A. Drits, "Mixed-layer kaolinite-montmorillonite: a comparison of observed and calculated diffraction patterns," *Clays and Clay Minerals*, vol. 21, no. 1, pp. 15–17, 1973.

[104] A. B. H. Amara, "X-ray diffraction, infrared and TGA/DTG analysis of hydrated nacrite," *Clay Minerals*, vol. 32, no. 3, pp. 463–470, 1997.

[105] A. U. Dogan, M. Dogan, M. Onal, Y. Sarikaya, A. Aburub, and D. E. Wurster, "Baseline studies of the clay minerals society source clays: specific surface area by the Brunauer Emmett Teller (BET) method," *Clays and Clay Minerals*, vol. 54, no. 1, pp. 62–66, 2006.

[106] C. D. Hatch, J. S. Wiese, C. C. Crane, K. J. Harris, H. G. Kloss, and J. Baltrusaitis, "Water adsorption on clay minerals as a function of relative humidity: application of BET and Freundlich adsorption models," *Langmuir*, vol. 28, no. 3, pp. 1790–1803, 2012.

[107] T. Kozaki, T. Sawaguchi, A. Fujishima, and S. Sato, "Effect of exchangeable cations on apparent diffusion of Ca^{2+} ions in Na- and Ca-montmorillonite mixtures," *Physics and Chemistry of the Earth, Parts A/B/C*, vol. 35, no. 6-8, pp. 254–258, 2010.

[108] S. Babel and T. A. Kurniawan, "Low-cost adsorbents for heavy metals uptake from contaminated water: a review," *Journal of Hazardous Materials*, vol. 97, no. 1-3, pp. 219–243, 2003.

[109] F. Bergaya and G. Lagaly, "Chapter 1 general introduction: clays, clay minerals, and clay science," *Developments in Clay Science*, vol. 1, pp. 1–18, 2006.

[110] R. D. Shannon, "Revised effective ionic radii and systematic studies of interatomic distances in halides and chalcogenides," *Acta Cryst*, vol. 32, no. 5, pp. 751–767, 1976.

[111] E. Ferrage, C. A. Kirk, G. Cressey, and J. Cuadros, "Dehydration of ca-montmorillonite at the crystal scale. Part I: structure evolution," *American Mineralogist*, vol. 92, no. 7, pp. 994–1006, 2007.

[112] E. Ferrage, C. A. Kirk, G. Cressey, and J. Cuadros, "Dehydration of ca-montmorillonite at the crystal scale. Part 2. Mechanisms and kinetics," *American Mineralogist*, vol. 92, no. 7, pp. 1007–1017, 2007.

[113] R. Chalghaf, W. Oueslati, M. Ammar, H. B. Rhaiem, and A. B. H. Amara, "Effect of an "in situ" hydrous strain on the ionic exchange process of dioctahedral smectite: case of solution containing (Cu^{2+}, Co^{2+}) cations," *Applied Surface Science*, vol. 258, no. 22, pp. 9032–9040, 2012.

[114] M. Meftah, W. Oueslati, N. Chorfi, and A. B. H. Amara, "Intrinsic parameters involved in the synthesis of metakaolin based geopolymer: microstructure analysis," *Journal of Alloys and Compounds*, vol. 688, pp. 946–956, 2016.

[115] M. Meftah, W. Oueslati, N. Chorfi, and A. B. H. Amara, "Effect of the raw material type and the reaction time on the synthesis of halloysite based zeolite Na-P1," *Results in Physics*, vol. 7, pp. 1475–1484, 2017.

[116] S. Caillère, S. Hénin, and M. Rautureau, "Minéralogie des argiles," *Classification et Nomenclature*, vol. 1982, no. 8, p. 184, 1982.

[117] G. W. Brindley, "Ethylene glycol and glycerol complexes of smectites and vermiculites," *Clay Minerals*, vol. 6, no. 4, pp. 237–259, 1966.

[118] R. C. Mackenzie, "The classification of soil silicates and oxides," *In Soil Components. Springer*, vol. 2, pp. 1–25, 1975.

[119] G. Pédro, *Les minéraux argileux dans Pédologie (2-Constituants et propriétés du sol)*, Eds. Duchaufour Ph. et Southier B, 1994.

[120] P. Komadel, J. Bujdák, J. Madejová, V. Šucha, and F. Elsass, "Effect of non-swelling layers on the dissolution of reduced-charge montmorillonite in hydrochloric acid," *Clay Minerals*, vol. 31, no. 3, pp. 333–345, 1996.

[121] F. B. K. G. Bergaya and G. Lagaly, "General introduction: clays, clay minerals, and clay science," *In Developments in Clay Science, Elsevier*, vol. 5, pp. 1–19, 2013.

[122] L. Sun, J. T. Hirvi, T. Schatz, S. Kasa, and T. A. Pakkanen, "Estimation of montmorillonite swelling pressure: A molecular dynamics approach," *The Journal of Physical Chemistry C*, vol. 119, no. 34, pp. 19863–19868, 2015.

[123] S. J. Gregg, K. S. W. Sing, and H. W. Salzberg, "Adsorption surface area and porosity," *Journal of the Electrochemical Society*, vol. 114, no. 11, p. 279C, 1967.

[124] L. Yu, W. L. Hsu, J. A. Shamim, and H. Daiguji, "Pore network modeling of a solid desiccant for dehumidification

applications," *International Journal of Heat and Mass Transfer*, vol. 186, article 122456, 2022.

[125] P. Pang, H. Han, L. Hu, C. Guo, Y. Gao, and Y. Xie, "The calculations of pore structure parameters from gas adsorption experiments of shales: which models are better?," *Journal of Natural Gas Science and Engineering*, vol. 94, article 104060, 2021.

[126] J. C. Groen, L. A. Peffer, and J. A. Moulijn, "Pore size determination in modified micro- and mesoporous materials. Pitfalls and limitations in gas adsorption data analysis," *Microporous and Mesoporous Materials*, vol. 60, no. 1-3, pp. 1–17, 2003.

[127] E. P. Barrett, L. G. Joyner, and P. P. Halenda, "The determination of pore volume and area distributions in porous substances. I. Computations from nitrogen isotherms," *Journal of the American Chemical Society*, vol. 73, no. 1, pp. 373–380, 1951.

[128] T. Liu, L. Ju, Y. Zhou et al., "Effect of pore size distribution (PSD) of Ni- Mo/Al_2O_3 catalysts on the Saudi Arabia vacuum residuum hydrodemetallization (HDM)," *Catalysis Today*, vol. 271, pp. 179–187, 2016.

[129] K. Sing, "The use of nitrogen adsorption for the characterisation of porous materials," *Colloids and Surfaces A: Physicochemical and Engineering Aspects*, vol. 187, pp. 3–9, 2001.

[130] P. Kumar, R. V. Jasra, and T. S. Bhat, "Evolution of porosity and surface acidity in montmorillonite clay on acid activation," *Industrial and Engineering Chemistry Research*, vol. 34, no. 4, pp. 1440–1448, 1995.

[131] J. M. Zielinski and L. Kettle, "Physical characterization: surface area and porosity," *London: Intertek*, vol. 23, p. 724, 2013.